# Use of X-Band Differential Reflectivity Measurements to Study Shallow Arctic Mixed-Phase Clouds

MARIKO OUE

*Department of Meteorology, The Pennsylvania State University, University Park, Pennsylvania*

MICHELE GALLETTI

*Biological, Environmental and Climate Sciences Department, Brookhaven National Laboratory, Upton, New York*

JOHANNES VERLINDE

*Department of Meteorology, The Pennsylvania State University, University Park, Pennsylvania*

ALEXANDER RYZHKOV

*Cooperative Institute for Mesoscale Meteorological Studies, University of Oklahoma and National Severe Storms Laboratory, Norman, Oklahoma*

YINGHUI LU

*Department of Meteorology, The Pennsylvania State University, University Park, Pennsylvania*

(Manuscript received 16 June 2015, in final form 25 October 2015)

ABSTRACT

Microphysical processes in shallow Arctic precipitation clouds are illustrated using measurements of differential reflectivity $Z_{DR}$ from the U.S. Department of Energy Atmospheric Radiation Measurement Program polarimetric X-band radar deployed in Barrow, Alaska. X-band hemispheric range height indicator scans used in conjunction with Ka-band radar and lidar measurements revealed prolonged periods dominated by vapor depositional, riming, and/or aggregation growth. In each case, ice precipitation fell through at least one liquid-cloud layer in a seeder–feeder situation before reaching the surface. A long period of sustained low radar reflectivity $Z_H$ (<0–5 dB$Z$) and high $Z_{DR}$ (6–7.5 dB) throughout the depth of the cloud and subcloud layer, coinciding with observations of large pristine dendrites at the surface, suggests vapor depositional growth of large dendrites at low number concentrations. In contrast, $Z_{DR}$ values decreased to 2–3 dB in the mean profile when surface precipitation was dominated by aggregates or rimed dendrites. Small but consistent differences in zenith Ka-band radar Doppler velocity and lidar depolarization measurements were found between aggregation- and riming-dominated periods. The clean Arctic environment can enhance $Z_{DR}$ signals relative to more complex midlatitude cases, producing higher values.

## 1. Introduction

Mixed-phase clouds, here defined as clouds composed of supercooled liquid drops and ice crystals within the same cloudy volume, are frequently observed in the Arctic. These Arctic mixed-phase clouds have been observed at temperatures as low as −30°C and colder (Witte 1968; Hobbs and Rangno 1998; Intrieri et al. 2002) and are unique in that they often persist for long periods, even up to a couple of weeks (Curry et al. 1996; Intrieri et al. 2002), despite the presence of persistent ice precipitation. Supercooled liquid drops at such low temperatures are possible only in relatively clean environments where low aerosol particle concentrations limit the liquid and snow precipitation efficiencies, leading to longer-lived clouds. Morrison et al. (2012) provides an excellent summary of the current understanding of lower-troposphere,

*Corresponding author address*: Mariko Oue, Department of Meteorology, The Pennsylvania State University, 503 Walker Bldg., University Park, PA 16802.
E-mail: muo15@psu.edu

DOI: 10.1175/JAMC-D-15-0168.1

single-layer, mixed-phase Arctic clouds. These clouds are often found in the stably stratified lower troposphere where interactions among formation and growth of ice and cloud drops, cloud-top radiative cooling, turbulence, and entrainment across cloud boundaries produce resilient clouds. However, our understanding of ice growth microphysics in the complex multilayer mixed-phase clouds is still lacking, largely because of a dearth of detailed observations of the ice growth processes contributing to the observed characteristics of these clouds.

The processes that govern the growth of ice particles in these Arctic mixed-phase clouds are vapor deposition, riming, and aggregation. In mixed-phase conditions, ice crystal growth rates are accelerated because ice crystals grow at the expense of cloud droplets through vapor deposition and collection. Depending on the specifics of the cloudy volume state [i.e., temperature, humidity (supersaturation ratio), updraft speed, and ice growth processes] a variety of ice crystal habits can be produced in these clouds. Compared to lower-latitude mixed-phase clouds, the range of crystal habit variability is somewhat more restricted in these weakly forced Arctic shallow clouds. During the fall and spring transition seasons, when mixed-phase clouds are most common in the Arctic, the majority of shallow cloud layers exist in temperature ranges conducive to planar primary habits (de Boer et al. 2009). In situ observations in these clouds reveal typically low liquid water contents ($<0.3\,\mathrm{g\,m^{-3}}$; Jayaweera and Ohtake 1973; Hobbs and Rangno 1998; McFarquhar et al. 2007), low ice water contents ($<0.1\,\mathrm{g\,m^{-3}}$; McFarquhar et al. 2007; Avramov et al. 2011), and low concentrations of ice nuclei ($<1\,\mathrm{L^{-1}}$; e.g., Radke et al. 1976; Fountain and Ohtake 1985; Bigg 1996; Pinto et al. 2001; Prenni et al. 2009) and ice crystals ($<1\,\mathrm{L^{-1}}$ in spring and $<10\,\mathrm{L^{-1}}$ in fall; Hobbs and Rangno 1998; McFarquhar et al. 2007; Avramov et al. 2011) relative to midlatitude environments. As a result, vapor depositional growth is often the dominant ice growth process in these shallow clouds, but riming and aggregation also occur in stronger precipitating systems (e.g., Shupe et al. 2008b; Avramov et al. 2011). The impact of the low ice water content in these clouds is reflected in typical lower radar reflectivity values (mostly less than 0–10 dB$Z$; e.g., Shupe et al. 2008a; Morrison et al. 2012) than in the midlatitude clouds, even in deeper precipitating systems (Verlinde et al. 2013).

The recent deployment of a polarimetric X-band weather radar by the U.S. Department of Energy (DOE) Atmospheric Radiation Measurement (ARM) Climate Research Facility in Barrow on the North Slope of Alaska (NSA) introduced a new tool to explore the microphysical processes in Arctic clouds (Bharadwaj et al. 2011). The measurement of polarimetric variables (e.g., differential reflectivity $Z_{\mathrm{DR}}$, differential propagation phase shift $\varphi_{\mathrm{DP}}$, and correlation coefficient $\rho_{\mathrm{HV}}$) by scanning radars offers the capability of documenting the spatial variability in ice particle characteristics (e.g., Straka and Zrnić 1993; Vivekanandan et al. 1999; Liu and Chandrasekar 2000; Zrnić et al. 2001; Dolan and Rutledge 2009; Park et al. 2009; Thompson et al. 2014).

Differential reflectivity $Z_{\mathrm{DR}}$ is the ratio of reflectivity factors in the horizontal $Z_H$ and vertical $Z_V$ polarizations. It is defined (Seliga and Bringi 1976) as

$$Z_{\mathrm{DR}} = Z_H - Z_V, \tag{1}$$

where $Z_H$ and $Z_V$ are expressed in logarithmic scale. The differential reflectivity $Z_{\mathrm{DR}}$ is an indicator of the reflectivity-weighted mean shape of particles in the resolution volume, and the magnitude of $Z_{\mathrm{DR}}$ is dependent on the particle ice mass, size, shape (and hence bulk density), and orientation of individual particles. Because $Z_{\mathrm{DR}}$ is a ratio, it is independent of particle number concentration. For nonspherical particles with a preferred orientation, $Z_{\mathrm{DR}}$ is a function of the radar elevation; for instance, planar crystals have highest $Z_{\mathrm{DR}}$ values at 0° (side incidence) and lowest at 90° (vertical incidence) elevation angles (e.g., Matrosov 1991; Aydin and Tang 1997; Matrosov et al. 2001; Wolde and Vali 2001; Westbrook 2014). The intensity of elevation dependency and the maximal $Z_{\mathrm{DR}}$ value at the lowest angle can be utilized using depolarization to distinguish different types of ice crystals and between planar crystals, rimed crystals, and aggregates (e.g., Matrosov 1991; Aydin and Tang 1997; Matrosov et al. 2001).

The specific differential phase $K_{\mathrm{DP}}$ is defined by the gradient of the one-way differential propagation phase shift $\varphi_{\mathrm{DP}}$:

$$K_{\mathrm{DP}} = \frac{\varphi_{\mathrm{DP}}(r_2) - \varphi_{\mathrm{DP}}(r_1)}{2(r_2 - r_1)}, \tag{2}$$

where $r$ is the distance from the radar ($r_1 < r_2$); $K_{\mathrm{DP}}$ depends on the aspect ratio, bulk density, number concentration, and orientation of particles (e.g., Doviak and Zrnić 1993; Ryzhkov and Zrnić 1998; Bringi and Chandrasekar 2001); and $\rho_{\mathrm{HV}}$ is defined by using the backscattering covariance matrix elements at horizontal $S_{\mathrm{HH}}$ and vertical $S_{\mathrm{VV}}$ polarizations (e.g., Doviak and Zrnić 1993; Zrnić et al. 1994) as follows:

$$\rho_{\mathrm{HV}} = \frac{|\langle S_{\mathrm{VV}} S_{\mathrm{HH}}^{*} \rangle|}{\sqrt{\langle |S_{\mathrm{HH}}|^2 \rangle}\sqrt{\langle |S_{\mathrm{VV}}|^2 \rangle}}, \tag{3}$$

where angle brackets denote ensemble average and the asterisk denotes the complex conjugate. The quantity

$\rho_{HV}$ is representative of the variability of the scattering characteristics of ice particles in the radar resolution volume and is therefore affected by the variety in particle shapes, compositions, and orientations (e.g., Zrnić et al. 1994).

Studies of midlatitude cloud systems have revealed $Z_{DR}$ and $K_{DP}$ enhancements near the dendritic growth regime around the −15°C temperature level (Kennedy and Rutledge 2011; Andrić et al. 2013; Bechini et al. 2013; Schneebeli et al. 2013; Kumjian et al. 2014; Thompson et al. 2014; Williams et al. 2015; Schrom et al. 2015). The higher $Z_{DR}$ reflects a significant contribution to the total reflectivity by the oriented planar crystals, whereas the $K_{DP}$ enhancements indicate significant concentrations of dendritic particles. Aggregation and/or riming regions have increasing $Z_H$ but decreasing (or low) $Z_{DR}$ and $K_{DP}$ (e.g., Hall et al. 1984; Ryzhkov and Zrnić 1998). These midlatitude studies focused on deep cloud systems (>~4 km) with mature aggregation–riming processes that produce higher $Z_H$ (15–30 dB$Z$) than the Arctic clouds. Although scattering calculations show that planar crystals should produce high $Z_{DR}$ (5+ dB; Hall et al. 1984; Matrosov 1991; Vivekanandan et al. 1999; Westbrook 2014), the $Z_{DR}$ enhancements around −15°C in these midlatitude cases generally peak between 0.5 and 2 dB. These lower values may be attributed to the coexistence of dendrites with other larger, more spherical ice particles produced by advanced stages of aggregation and/or riming (Schrom et al. 2015).

The lower ice water contents and particle concentrations, and hence lower $Z_H$, in shallow Arctic clouds around the dendritic growth regime suggest that the dominant polarimetric signature should be in $Z_{DR}$. Low number concentrations of planar crystals produce only small accumulated phase shifts, making $K_{DP}$ difficult to measure at X band. We show how polarimetric radar measurements combined with the extensive suite of DOE ARM measurements can be used to illuminate the microphysical processes in shallow Arctic clouds.

## 2. Data and methodology

The DOE ARM X-band scanning precipitation radar (X-SAPR) at Barrow (Fig. 1) collects polarimetric measurements through simultaneous transmission and simultaneous reception of horizontally and vertically linearly polarized waves (STSR hybrid mode). The characteristics of the system are provided in Table 1. The data used in this study were collected during the NSA Radar Intensive Observing Period (1–7 May 2013; http://www.arm.gov/campaigns/nsa2013nsasr), one of the objectives of which was to assess the quality of the observations under a variety of sampling modes. Therefore, the sampling modes of the radar were systematically

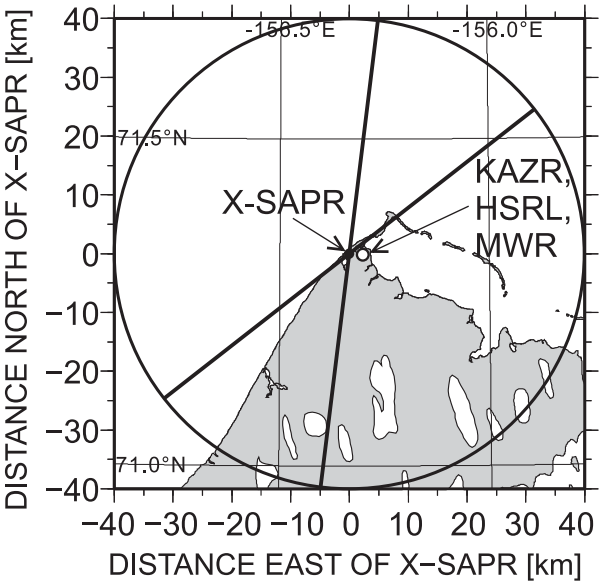


FIG. 1. Map of the Barrow region with the locations of the X-SAPR, KAZR, HSRL, and MWR indicated. The two black lines crossing the X-SAPR site represent HRHI directions used in this study. The large circle represents the observation range during the IOP.

varied throughout the period. This study presents results from hemispheric range height indicator (HRHI) scans taken from two long-lasting precipitation events. Three HRHI scans were selected for detailed analysis on the basis of the availability of ice precipitation particles photographs and persistence of the observed $Z_{DR}$ fields aloft. The radar operating–sampling modes for each are listed in Table 2.

Polarimetric radars often have a systematic bias in $Z_{DR}$ (Seliga et al. 1981). There may be additional noise-related biases in $Z_{DR}$ (Gourley et al. 2006) and $\rho_{HV}$ (Bringi et al. 1983) for low signal-to-noise ratios. Oue et al. (2015) provide a detailed discussion of the corrections applied to the data used in this study. The systematic $Z_{DR}$ bias for the current data was +0.94 dB. The $K_{DP}$ was estimated from the smoothed differential propagation phase shift $\varphi_{DP}$ using the iterative algorithm proposed by Hubbert and Bringi (1995). The $Z_{DR}$ dependence on elevation angle was determined from the HRHI scans. To minimize the effect of noise on the $Z_{DR}$ measurements, we present mean $Z_{DR}$ as a function of elevation angle averaged over 5° elevation angle increments and reported at the center elevation of each interval.

The surface precipitation photographs were taken approximately 0.3 km west of the radar. These photographs served as the basis for interpretation of $Z_H$ and $Z_{DR}$ from the HRHIs. The NSA ARM Ka-band zenith radar (KAZR), the high-spectral-resolution lidar (HSRL),

TABLE 1. The DOE ARM X-SAPR specifications.

| Parameter | Value |
|---|---|
| Site | |
| Location | Barrow, AK |
| Lat (°N) | 71.325 |
| Lon (°E) | −156.668 |
| Alt (m) | 32 |
| Transmitter | |
| Type | Magnetron |
| Center frequency (MHz) | 9600 |
| Peak power (kW) | 200 |
| Polarization | H + V |
| Duty cycle (%) | 0.1 |
| Max pulse width ($\mu$s) | 2.0 |
| Max PRF (kHz) | 2.3 |
| Antenna and pedestal | |
| Antenna diameter (m) | 2.4 |
| 3-dB beamwidth | 1.0 |
| Gain (dB) | 45 |
| Max scan rate (° $s^{-1}$) | 36.0 |
| Receiver | |
| Analog-to-digital converter (bits) | 16 |
| Polarization | H + V |
| Noise figure (dB) | <3.0 |
| Intermediate frequency sampling (MHz) | 80 |
| Range gate spacing (m) | 50–250 |
| Range (km) | 40 |
| Decimation | Adjustable |
| Receiver bandwidth (MHz) | Adjustable |
| H + V | Simultaneous transmit and simultaneous receiver of horizontal (H) and vertical (V) polarized signals |

the microwave radiometer (MWR), and the balloon-borne sounding system were used to provide more information about the details of the observed cloud systems. These instruments were located 2.2 km east of the X-SAPR (Fig. 1). The vertically pointing KAZR (Bharadwaj et al. 2011) measured continuous profiles of reflectivity, mean Doppler velocity, and Doppler spectrum width in the column above the radar. The HSRL (Eloranta 2005) was used to identify liquid-cloud layers. Generally, a combination of high lidar backscattering coefficient ($>10^{-4}\,m^{-1}\,sr^{-1}$) and low lidar depolarization signals (<4%) is attributed to liquid cloud (e.g., Sassen 1991). We used the MWR liquid water path (LWP) retrievals from the statistical method developed by Liljegren et al. (2001). Cloud base was indicated by a Vaisala ceilometer.

Sometimes, in thick liquid-cloud layers, the HSRL beam was completely attenuated before reaching cloud top. In such situations, the tops of liquid-cloud layers embedded in ice precipitation were inferred, when possible, from vertical gradients in the KAZR Doppler radar spectrum width (Shupe et al. 2004). We evaluated this approach by comparing 20-min average profiles of KAZR spectrum width and HSRL backscattering coefficient and depolarization measurements around the time of the 1730 UTC ARM radiosonde release (Fig. 2). The largest gradient in KAZR spectrum width occurs in the 1.4–1.5-km altitude (~0.05 m $s^{-1}$ per 100 m, horizontal dashed line) and is closely associated with a maximum in relative humidity at the bottom of an inversion later and on top of a layer of high HSRL backscattering coefficient ($>10^{-4}\,m^{-1}\,sr^{-1}$) and low depolarization ratio (<4%). Cloud top was defined as the last range gate where the gradient exceeded 0.0004 $s^{-1}$.

Intercomparisons of X-SAPR and KAZR radar reflectivities showed that the KAZR reflectivities were approximately 2–5 dB larger than the X-SAPR during the IOP. Because absolute calibrations of both radar reflectivities have not been done, the radar reflectivities from both radars in this study are used to describe qualitative characteristics.

To aid interpretation of the radar measurements, we used X-band (9.41 GHz) scattering properties of realistic ice crystals from the database initiated by Botta et al. (2013) and updated by Lu et al. (2014, their section 4.1) and for aggregates by Botta et al. (2011). The scattering properties of these particles were calculated using the general multiparticle Mie method (GMM; Xu 1995) for incident angles from 0° to 90° in 10° increments. Canting effects were not taken into account. Only planar ice crystals from the crystal database, with different shapes, sizes, thicknesses, and masses, were used in this study. Aggregates in the database were represented by collections of pristine stellar crystals (Botta et al. 2011). The constituent pristine crystals had random orientation, position, and size. All aggregates were constrained to fit in two general categories based on mass–dimensional relationships, one

TABLE 2. Observational settings of the X-SAPR HRHI scans used in this study.

| | Pulse repetition frequency (Hz) | Pulse width ($\mu$s) | Range gate spacing (m) | No. of integrated pulses | Scan rate (° $s^{-1}$) | Azimuth angle (°) |
|---|---|---|---|---|---|---|
| 1554 UTC 2 May 2013 | 1950 | 0.50 | 75 | 256 | 2 | 7 |
| 1838 UTC 2 May 2013 | 1950 | 0.50 | 75 | 162 | 6 | 7 |
| 1057 UTC 6 May 2013 | 1950 | 0.50 | 75 | 256 | 2 | 52 |

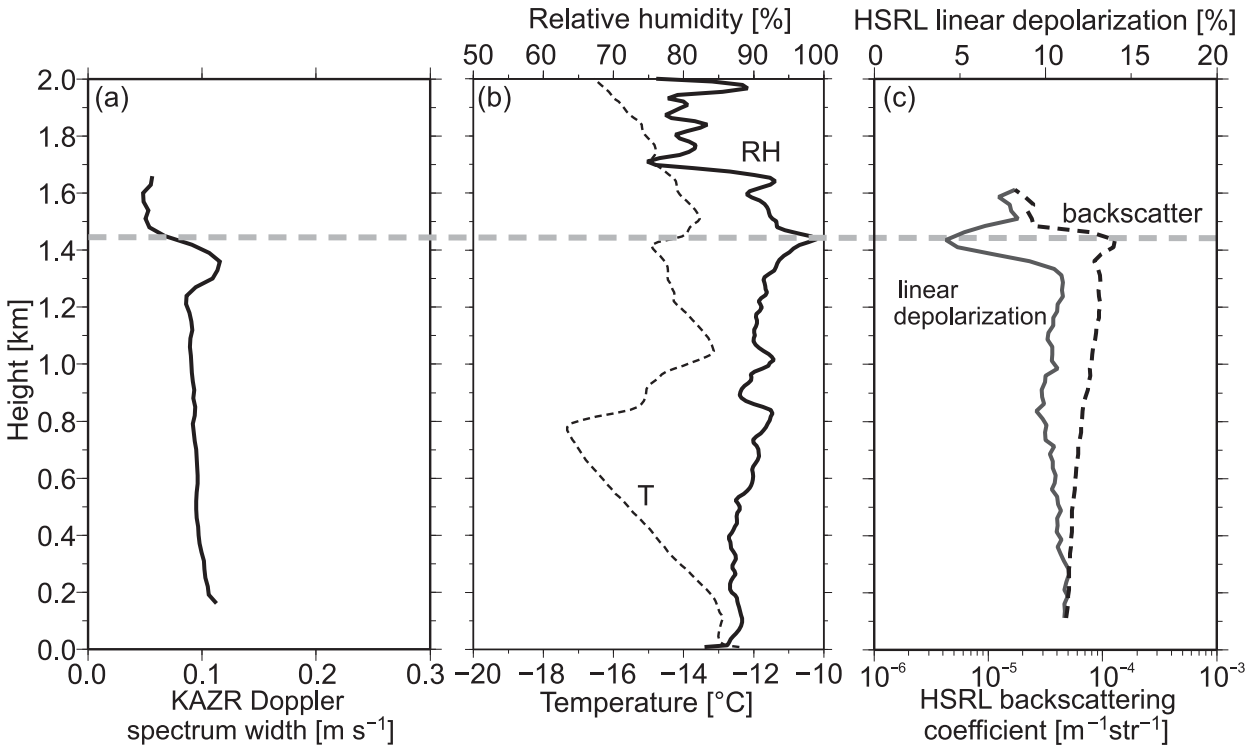


FIG. 2. Vertical profiles of (a) KAZR Doppler spectrum width, (b) temperature (dashed line) and relative humidity (solid line), and (c) HSRL backscattering coefficient (dashed line) and linear depolarization ratio (solid line). The KAZR and HSRL profiles are 20-min averages spanning the radiosonde release at 1730 UTC 2 May. We identify the liquid-cloud top with the horizontal dashed line.

for aggregates of dendrites (denoted as lower density; Kajikawa 1989) and the other for aggregates of thin plates (denoted as higher density; Mitchell et al. 1990). At a given maximum dimension, the Kajikawa (1989) relationship produced relatively lower bulk densities and aspect ratios of the modeled aggregates compared to the Mitchell et al. (1990) relationship (Botta et al. 2011). Aggregates were assumed to fall with their maximum dimension aligned horizontally.

## 3. Observational analysis

The photographs taken at the surface suggested that precipitation growth processes aloft were dominated by vapor deposition, aggregation, or rime growth of dendrites over extended periods of time in each case. Three cases occurred during two long-lasting precipitation events: a shallow boundary layer cloud system on 2 May 2013 and a frontal system on 6 May 2013. Such precipitation events have frequently been observed at Barrow (e.g., Shupe et al. 2006; Morrison et al. 2011, 2012; Verlinde et al. 2013). The 2 May case produced two precipitation categories, pristine dendrites and aggregates of dendrites, and the 6 May case produced rimed dendrites.

### a. *Case of 2 May 2013*

On 2 May 2013 a weak surface trough extended from north of the Canadian Archipelago region toward Barrow. Early in the day, a mixed-phase cloud layer with cloud tops at 1.5 km produced light precipitation at Barrow (Fig. 3a, KAZR). As the weak surface trough approached Barrow, more clouds at multiple different layers became apparent over Barrow. From 1400 UTC through 2000 UTC, higher reflectivity precipitation (12 dB$Z$) from a cloud layer just below 1.8 km was observed, while several other nonprecipitating cloud layers are present above 2 km. During the higher reflectivity period, LWP retrievals (Fig. 3b) registered 10–15 g m$^{-2}$. Although these LWP values are below the uncertainty of the retrieval (25 g m$^{-2}$; Turner 2005), they are consistent with the LWP retrieved from the G-band vapor radiometer profiler (M. Cadeddu 2015, personal communication), which is more sensitive to the presence of liquid (retrieval uncertainty of ~8 g m$^{-2}$; Cadeddu et al. 2009). This case is characteristic of many NSA precipitation events, where ice forms and precipitates from tenuous supercooled liquid-cloud layers that comprise the mixed-phase regions of the cloud (e.g., Shupe et al. 2006; Verlinde et al. 2013). Here, we refer to these

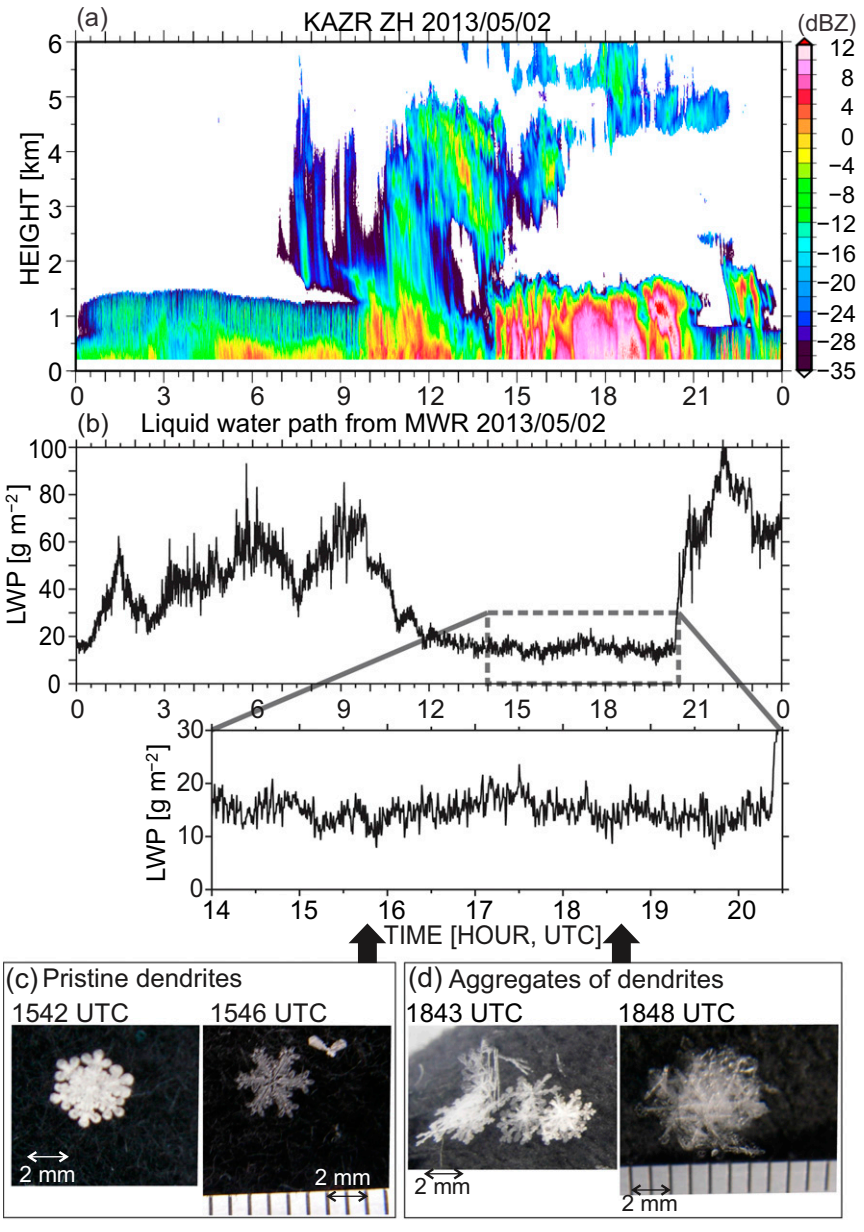


FIG. 3. (a) Time-vs-height cross section of KAZR radar reflectivity, (b) time series of liquid water path retrieved from the MWR measurements, and photographs of (c) pristine dendrites and (d) aggregates of dendrites (ruler ticks are millimeters) on 2 May 2013. Particle photographs in (c) were taken at 1542 and 1546 UTC, and those in (d) were taken at 1843 and 1848 UTC.

embedded mixed-phase regions as liquid-cloud layers to emphasize the presence of liquid water.

Figure 4 reveals the thermodynamic structure over Barrow at 1730 UTC on that day. The shaded regions represent ice-supersaturated altitudes. Most of the atmosphere below 1.8 km is supersaturated with respect to ice, implying that ice precipitation is growing via vapor deposition as it is falling to the surface. The entire profile below the cloud top has temperatures ranging between −12° and −18°C. Pristine crystal growth in this temperature range yields either plates or dendrites (Magono and Lee 1966), depending on the supersaturation conditions (low-supersaturation-yielding plates; high-supersaturation-yielding dendrites).

Photographs of the precipitation particles taken during the early period (1400–1700 UTC) reveal a mixture

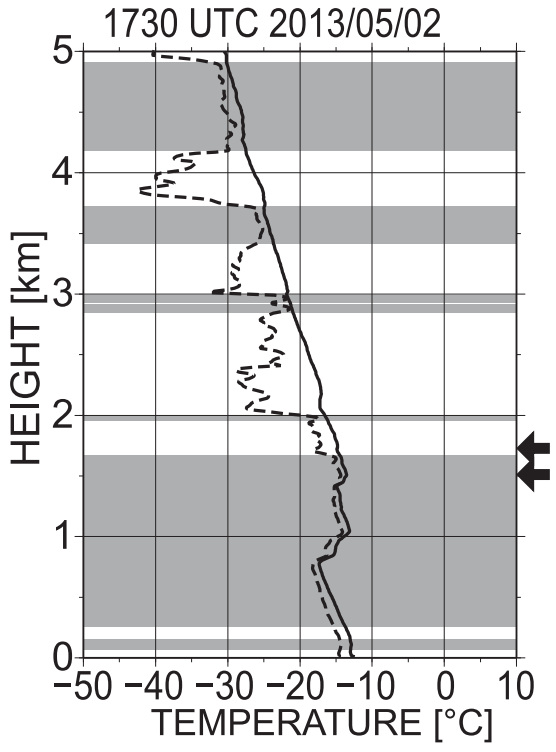


FIG. 4. Vertical profiles of temperature (solid line) and dewpoint temperature (dashed line) from the Barrow soundings at 1730 UTC 2 May 2013. Shaded regions represent supersaturation conditions with respect to ice. Arrows denote liquid-cloud tops for the pristine dendrite case (1.75 km) and the aggregate case (1.5 km).

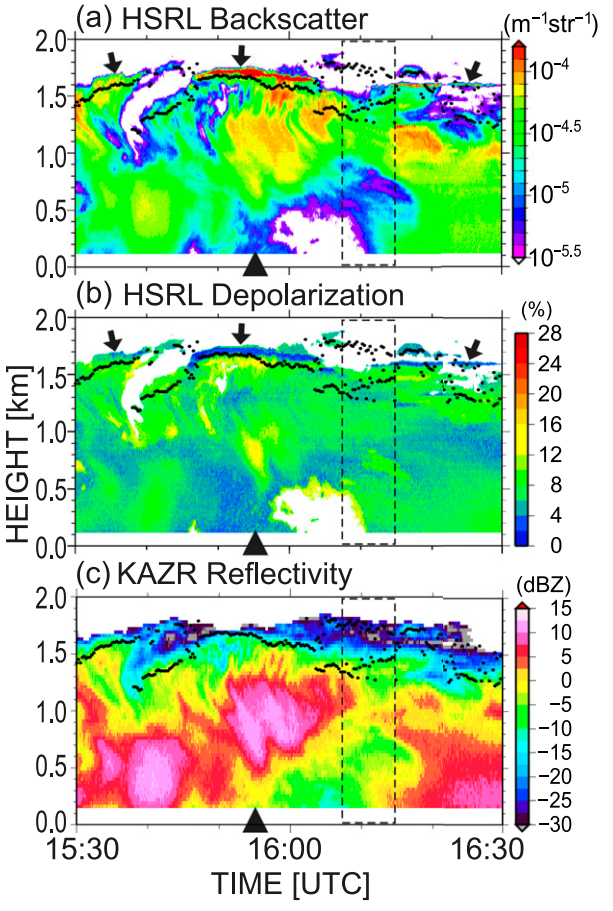


FIG. 5. Pristine dendrite case on 2 May 2013 time-vs-height cross sections of HSRL (a) backscatter and (b) linear depolarization ratio and KAZR (c) radar reflectivity. The black triangles indicate the time of the X-SAPR HRHI scan. The small black dots in (a)–(c) represent cloud base observed by a ceilometer. The black arrows denote the HSRL-indicated liquid-cloud layers. The rectangular region enclosed by the dashed lines is used for mean profiles in Fig. 18, below.

of different pristine planar crystal habits, such as dendrites, sector plates, and stellar crystals (Fig. 3c). Collectively, we refer to these as dendrites. The observed pristine dendrites were large, with maximum dimensions up to 5 mm. Precipitation particles captured during the later period (1700–1900 UTC) were predominantly aggregates of dendrites. Because of this change, we discuss the pristine dendrite- and aggregate-dominated periods separately.

### 1) PRISTINE DENDRITE PERIOD

Because the LWP is below the retrieval uncertainty during the pristine dendrite period (Fig. 3b), we confirm the presence of liquid water clouds. The HSRL measurements indicate a thin (<100 m), intermittent liquid-cloud layer (backscatter $> 10^{-4}\,\mathrm{m^{-1}\,sr^{-1}}$ and linear depolarization ratio < 4%) embedded in the cloud system around 1.7-km altitude (Figs. 5a,b; denoted by arrows). The ceilometer-detected cloud bases (black dots) suggest other intermittent liquid-cloud layers at altitudes between 1.5 and 1.7 km. The higher, though still relatively low, linear depolarization ratios (mean over the hour <8%; maximum ~15%) with larger backscatter ($>10^{-4.5}\,\mathrm{m^{-1}\,sr^{-1}}$) below the liquid-cloud layers are consistent with scatter dominated by oriented, regularly shaped ice particles (i.e., plates or dendrites; Platt 1978; Sassen and Benson 2001; E. Eloranta 2015, personal communication). The KAZR reflectivity pattern (Fig. 5c) reveals the presence of another cloud layer at 1.7–1.9 km above the HSRL-observed liquid-cloud layer, suggesting that ice particles from that cloud layer fell into the liquid-cloud layers in a seeder–feeder scenario.

Figure 6 shows $Z_H$ and $Z_{DR}$ from the X-SAPR HRHI scan at 1554 UTC. The $Z_{DR}$ attains values greater than 6 dB in lower $Z_H$ regions (<0–5 dBZ). The $Z_{DR}$ variation with elevation angle is shown in Fig. 6c for three different constant altitude bands. At lower reflectivity values (< −15 dBZ) the $Z_{DR}$ measurement noise increased.

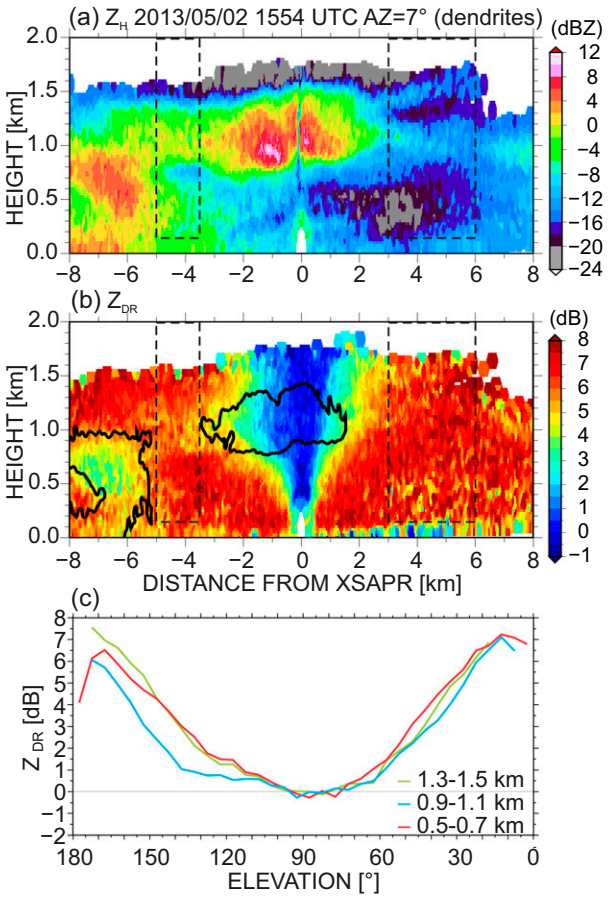


FIG. 6. X-SAPR HRHI scans of (a) $Z_H$ and (b) $Z_{DR}$ at 1554 UTC 2 May 2013 and (c) elevation angle vs $Z_{DR}$ at constant altitudes in the HRHI within a range of 8 km from the radar. Red, blue, and green lines represent heights of 0.5–0.7, 0.9–1.1, and 1.3–1.5 km, respectively. The $Z_{DR}$ values in (c) are averaged over 5° elevation angle increments and reported at the center elevation of each interval. The black contour in (b) represents isolines of $Z_H = 0$ dBZ. The rectangular regions enclosed by dotted lines in (a) and (b) are used for mean profiles in Fig. 17, below.

To see the intrinsic $Z_{DR}$ values unaffected by this noise, we applied a reflectivity threshold ($Z_H \geq -15$ dBZ) before averaging $Z_{DR}$ values in 200-m-thick height increments. The $Z_{DR}$ reaches extreme values of 6–7.5 dB at lower elevation angles <20° (>160°) at each height range. The $Z_{DR}$ values rapidly decrease with elevation angle to reach 0 dB at zenith. Such $Z_{DR}$ elevation dependence is what is expected from planar crystals that have highest $Z_{DR}$ values (7–9 dB) at side incidence and approach 0 dB at vertical incidence (e.g., Matrosov 1991; Aydin and Tang 1997; Westbrook 2014). The low $Z_H$, high $Z_{DR}$, and low HSRL linear depolarization ratio are consistent with sparse but fairly homogeneous populations of oriented, high-aspect-ratio pristine ice particles at all heights below the liquid-cloud base.

The general pattern revealed in Fig. 6 persisted for several hours. Figure 7 shows height-versus-time diagrams of the X-SAPR $Z_H$ and $Z_{DR}$ from 1400 UTC through 1915 UTC. During this period the X-SAPR performed a sequence of HRHI scans at three azimuth angles, each separated by 45°, every 5 min. Each profile represents the mean values of all points with elevation angles of 14°–15° (165°–166°) in 50-m height increments from all three HRHIs. This figure is similar to the quasi-vertical profiles introduced by Kumjian et al. (2013) and Ryzhkov et al. (2016). The elevation angle limitation was applied to ensure an equal number of points at all heights in the profile. A persistent signature of $Z_{DR}$ values exceeding 6 dB is evident close to cloud top, where $Z_H < -8$ dBZ. The $Z_{DR}$ mostly remained >5 dB in regions of $Z_H < -4$ dBZ within the lower cloud system from 1400 to 1700 UTC, spanning the period when mostly pristine crystals were observed at the surface. After 1700 UTC, the lower-level $Z_{DR}$ drops to approximately 2–3 dB even while $Z_H$ increases, suggesting a change in the dominant precipitation production process.

### 2) AGGREGATES OF DENDRITES PERIOD

The HSRL and KAZR measurements shown in Fig. 8 reveal a persistent altocumulus liquid-cloud layer at approximately 1.4–1.5 km (denoted by arrows 2 and 4) at the time of the photographs of aggregates of dendrites (Fig. 3d). The HSRL (Figs. 8a,b; arrows 1 and 3) indicates the presence of two other thin (~50 m) liquid-cloud layers in the 30 min prior to the surface observations of aggregates: one 100 m below the altocumulus layer and another above. The ceilometer-detected cloud base corresponds to the lower HSRL-indicated layer from 1805 to 1815 UTC, after which time the HSRL failed to detect liquid above the ceilometer-indicated cloud base. This discrepancy may result from low liquid drop concentrations in the presence of oriented ice particles. The presence of the HSRL-indicated liquid-cloud layer at 1.5 km is supported by the coincident rapid increase in the KAZR spectrum width at that height (Fig. 8d; gray line). Similar to the earlier dendrite-dominated period, precipitation particles from the topmost cloud layer fell into the embedded liquid-cloud layers in a seeder–feeder scenario. The HSRL linear depolarization below the liquid cloud (~12%; Fig. 8b) is higher than in the pristine dendrite case (<8%; Fig. 5b), consistent with what would be expected from the presence of some irregular-shaped aggregates mixed with pristine dendrites.

The X-SAPR HRHI at 1838 UTC (Fig. 9) reveals a distinct change in the $Z_H$ and $Z_{DR}$ patterns relative to

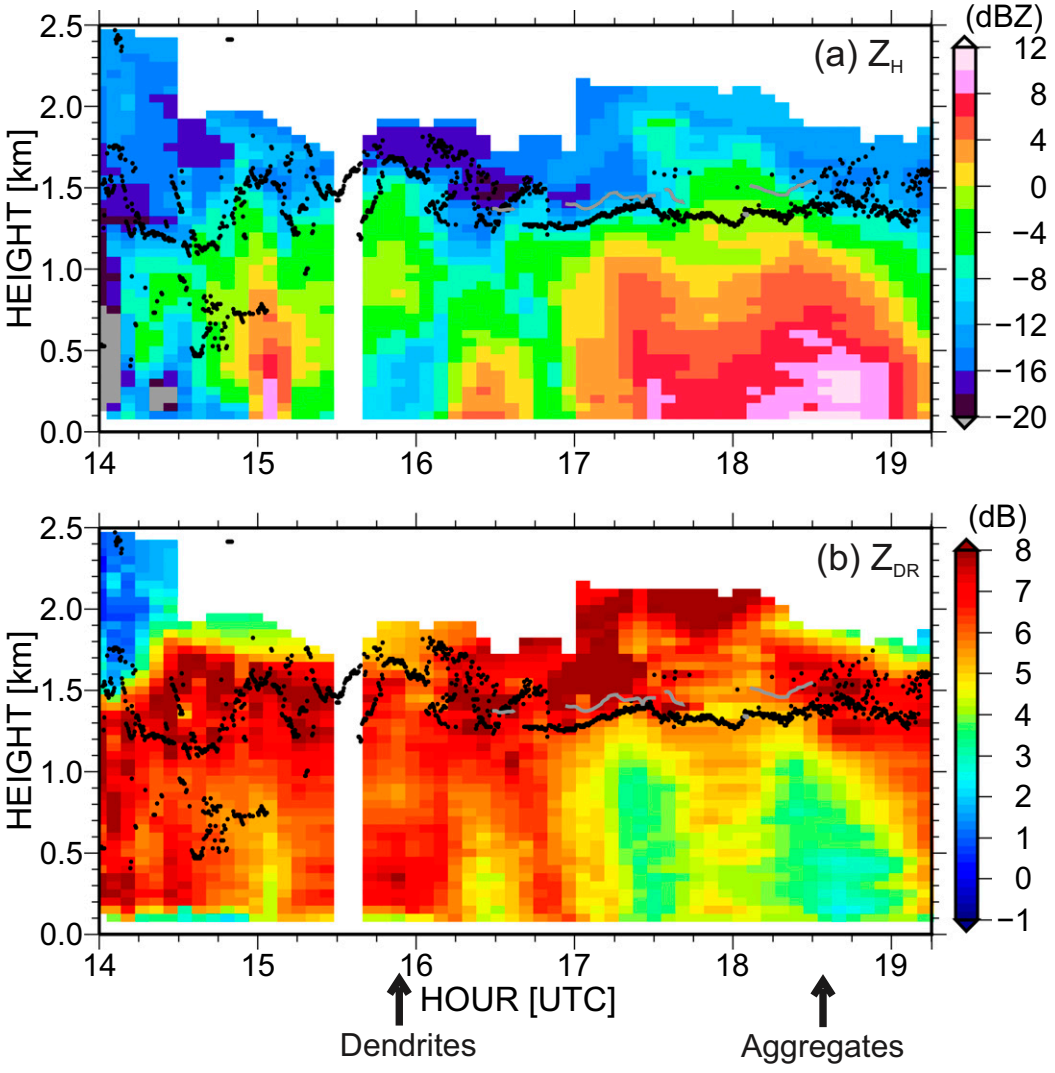


FIG. 7. Time-vs-height cross sections of the X-SAPR (a) $Z_H$ and (b) $Z_{DR}$ on 2 May 2013. Each profile represents the mean values of all points with elevation angles of 14°–15° (165°–166°) in 50-m height increments from three HRHI scans (azimuth angles of 7°, 52°, and 97°) every approximately 5 min. The horizontal gray lines and black dots respectively represent liquid-cloud top estimated from the KAZR Doppler spectrum width and cloud base observed by a ceilometer.

the earlier period. Below the height of the embedded liquid-cloud layers (1.4–1.5 km; Figs. 8a,b), the X-SAPR $Z_H$ structure is mostly horizontally uniform, increasing with decreasing altitude at lower altitudes. The $Z_{DR}$ attains maximum values of up to 7 dB near the echo top (Fig. 9b), similar to the earlier period, but decreases toward the surface. This altitude variation is captured in the composite $Z_{DR}$ profiles (Fig. 9c). The mean $Z_{DR}$ at and just below the lowest liquid-cloud layer (1.2–1.4 km, denoted by arrow 3 in Fig. 8a) is ~6 dB for elevation angles less than 10° (greater than 170°) but decreases to ~5 dB at 0.9–1.1 km, ~3 dB at 0.5–0.7 km, and ~2.5 dB at 0.1–0.3 km. The coexisting decrease in $Z_{DR}$ and increase in $Z_H$ going toward the surface below the liquid-cloud layers is consistent with the process of aggregation of ice crystals (Hall et al. 1984; Ryzhkov and Zrnić 1998; Kennedy and Rutledge 2011; Andrić et al. 2013; Bechini et al. 2013; Schrom et al. 2015). Figure 7 reveals that this change in the $Z_H$ and $Z_{DR}$ profiles occurred around 1700 UTC, when the reflectivity above the liquid-cloud layers (1.4–1.5 km) increased (also see Fig. 8c; 1830–1850 UTC). Although it is difficult to discern the exact cause of this $Z_H$ increase, it appears that a higher-level cloud advected over the radar site. The general pattern of $Z_H$ and $Z_{DR}$ profiles persisted until 1900 UTC, shortly after the small feature at 1.7 km disappeared.

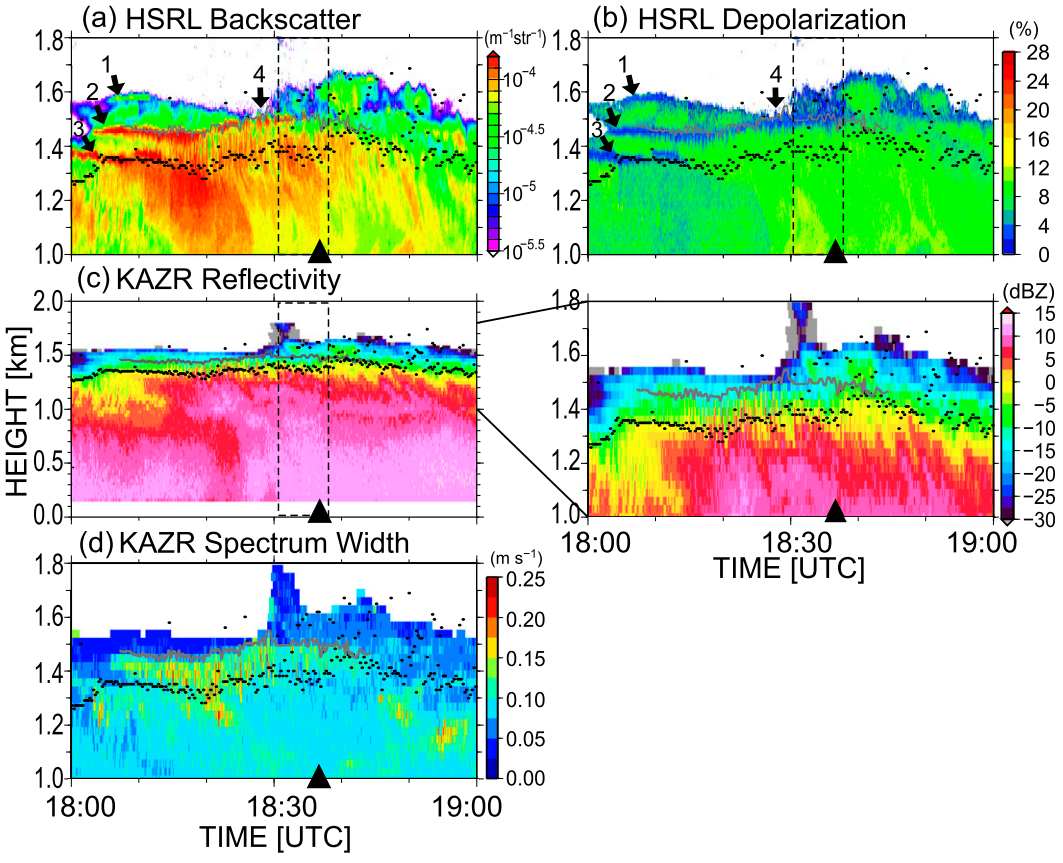


FIG. 8. Aggregates of the dendrites case on 2 May 2013 time-vs-height cross sections of HSRL (a) backscatter and (b) linear depolarization ratio, and KAZR (c) radar reflectivity and (d) Doppler spectrum width. The black triangles indicate the time of the X-SAPR HRHI scan. The black arrows denote the HSRL-indicated liquid-cloud layers. The small black dots in (a)–(d) represent cloud base observed by a ceilometer. The horizontal gray lines represent liquid-cloud top estimated from the KAZR Doppler spectrum width. The region enclosed by the dashed lines in (a)–(c) is used for mean profiles in Fig. 18, below.

### *b. Case of 6 May 2013*

On 6 May 2013, a slow-moving surface trough, extending southeast from a low in the Chukchi Sea, passed through Barrow from the southwest to northeast. Aloft, a broad 500-hPa trough approached from the west, passing over Barrow by 1800 UTC on 7 May. Surface precipitation started at 0600 UTC on 6 May from a shallow mixed-phase cloud system associated with the surface trough (cloud top of 1.5 km in Fig. 10). The cloud top gradually lifted to about 3 km later in the day as the trough line approached Barrow. Before 1230 UTC, this low-level precipitating system was well separated from the upper-level clouds associated with the 500-hPa trough (reflectivity above 3 km). The sounding profile at 1100 UTC (Fig. 11) reveals that the low-level precipitating cloud layer was situated just below an inversion at 2.2 km. The temperature at the bottom of this small inversion was −18°C in the planar crystal growth regime (Magono and Lee 1966). Photographs of precipitation particles revealed that lightly rimed dendrites (underlying crystal shape visible; maximum dimension 2–3 mm) dominated at the surface (Fig. 10c).

#### RIMED DENDRITE PERIOD

At the time when rimed dendrites were observed at the surface, the MWR-retrieved LWP was still relatively low at ~38 g m$^{-2}$ but was 3 times as high as during the previous cases (Fig. 10b). The HSRL revealed two persistent, 100–150-m-thick, liquid-cloud layers embedded in ice precipitation at 0.5- and 1.5-km altitudes between 1030 and 1100 UTC (Figs. 12a,b; denoted by arrows 1 and 2). Although the HSRL indicates that the liquid-cloud layer at 1.5-km (denoted by arrow 1) altitude dissipated at the time of the HRHI (indicated by a triangle), the precipitation fall streaks in both the HSRL and KAZR measurements suggest that the precipitation observed at the surface originated from that layer

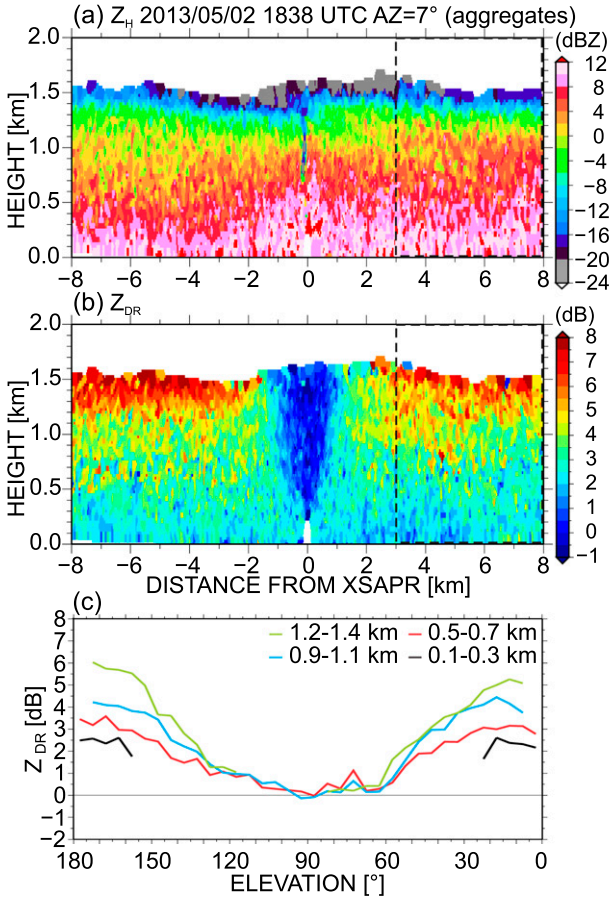


FIG. 9. As in Fig. 6, but for the aggregate case at 1838 UTC 2 May 2013. Here the lines in (c) represent heights of 0.1–0.3 km (black), 0.5–0.7 km (red), 0.9–1.1 km (blue), and 1.2–1.4 km (green). In the lowest height range, $Z_{DR}$ values are available only at elevation angles <20° or >160°. The regions inside the dashed rectangles in (a) and (b) are used for mean profiles in Fig. 17, below.

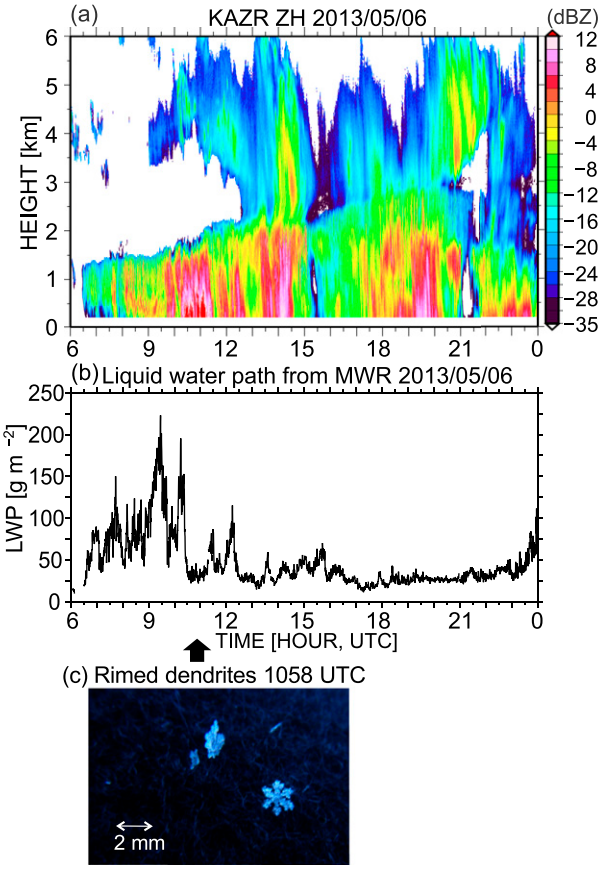


FIG. 10. As in Fig. 3, but for 6 May 2013. The photograph represents rimed dendrites taken at 1058 UTC.

(Figs. 12a,c). The KAZR reflectivities indicate the presence of an ice-seeding cloud layer (1.8–1.9 km, denoted by arrow 3) above the upper liquid-cloud layer. The reflectivity was enhanced when precipitation from the seeder-cloud encountered the upper liquid-cloud layer to produce fall streaks below the liquid-cloud layer. The HSRL fall streak backscatter (Fig. 12a) and linear depolarization values (Fig. 12b) are elevated above the background between the two liquid-cloud layers and experience a jump across the lowest liquid-cloud layer. The increase in the HSRL linear depolarization is consistent with the presence of highly irregular, rimed ice particles with high depolarization values (Sassen 1991) mixed with more regular dendrites and aggregates.

The X-SAPR HRHI $Z_H$ at 1057 UTC (Fig. 13a) captured the ice-generating seeder-cloud layer (1.6–2 km) above the 1.5–1.6-km liquid-cloud layer (arrow 1). The seeder echo-top height was 2.1 km. The $Z_H$ values increase with decreasing height, exceeding 12 dB$Z$ close to the surface. Smaller-scale (100–200 m, denoted by vertical arrows) streak-like $Z_H$ peaks near the upper liquid-cloud layer (altitude 1.3–1.5 km) merge together into larger-scale (horizontal scale 1.5–3 km, denoted by horizontal arrows) structures in the subcloud layer (altitude 0.6–1.3 km). The smaller-scale streaks in X-SAPR correspond to the HSRL- and KAZR-measured fall streaks originating from the dissipating liquid clouds (Fig. 12a; 1040–1100 UTC). Focusing on the rightmost larger-scale structure indicated in Fig. 13a, one can see that the $Z_{DR}$ values in the structure are lower compared to those between the three larger-scale structures and decrease with decreasing height. The $Z_{DR}$ attains its lowest values of ~2 dB at or below the top of the lower liquid-cloud layer.

The $Z_{DR}$ elevation angle dependence and its variation with altitude shown in Fig. 13c are similar to those in Fig. 9c. Values of $Z_{DR}$ in the seeder-cloud layer (green line in Fig. 13c; 1.6–1.8 km) are similar to those of the pristine dendrite case (Fig. 6c) and the aggregate case at 1.2–1.4 km (Fig. 9c), suggesting that the three cases have

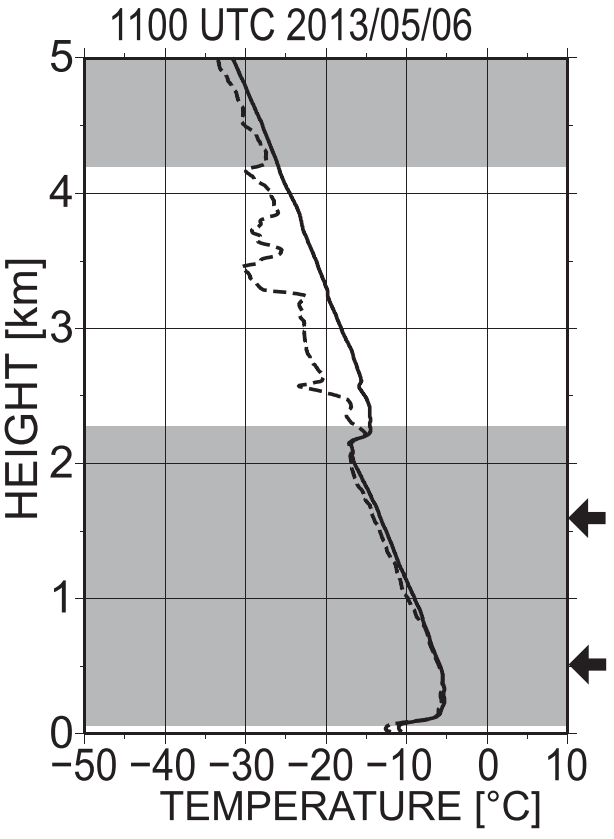


FIG. 11. As in Fig. 4, but for 1100 UTC on 6 May 2013. Arrows denotes embedded liquid-cloud tops for the rimed dendrite case.

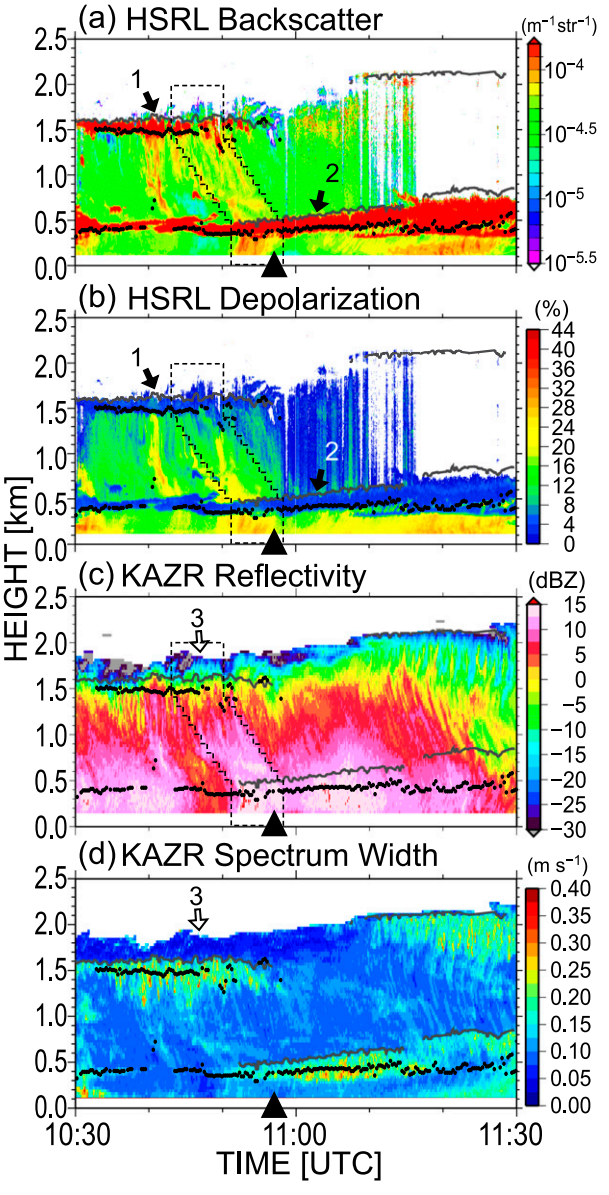


FIG. 12. As in Fig. 8, but for the rimed dendrite case on 6 May 2013. The black and white arrows denote the HSRL-indicated liquid-cloud layers and KAZR-observed seeder cloud, respectively.

similar ice crystal habits close to cloud top. The time evolution of the $Z_H$ and $Z_{DR}$ during this event is captured in the time series of quasi-vertical profiles constructed from the X-SAPR HRHIs from 0800 through 1300 UTC (Fig. 14). The $Z_H$ and $Z_{DR}$ profiles at the time when the rimed dendrites were observed persisted from 1000 through 1130 UTC, in association with the passage of a short-lived, more intense precipitation event. The change in pattern at 1130 UTC appears to be associated with the dissipation of the liquid-cloud layer at 1.5–1.6 km. After 1130 UTC, the $Z_H$ increases and $Z_{DR}$ decreases toward the surface at slower rates than those during the rimed dendrite period, suggesting a change in precipitation type. The $Z_H$ and $Z_{DR}$ pattern during the rimed dendrite period is similar to that during the aggregate period. We explore differences between the riming and aggregation cases in more detail in the discussion.

## 4. Evaluation of $Z_{DR}$ values by scattering calculations

We evaluate our interpretations of the observed $Z_{DR}$ by looking at horizontal-to-vertical backscatter cross-sectional ratios ($\sigma_{hh}/\sigma_{vv}$) from scattering calculations for single ice particles. All cross sections are average values for random orientations of the particle maximum dimension in the horizontal plane. Note that, while the $\sigma_{hh}/\sigma_{vv}$ corresponds to the $Z_{DR}$ for a single particle, the observed $Z_{DR}$ is reflectivity weighted by the particle size distribution in the radar resolution volume so that $\sigma_{hh}/\sigma_{vv}$ is not directly equivalent to $Z_{DR}$.

Figure 15 shows $\sigma_{hh}/\sigma_{vv}$ calculated in 10° elevation angle increments for four representative dendrite particles. These four dendrites (Fig. 15a), each with a

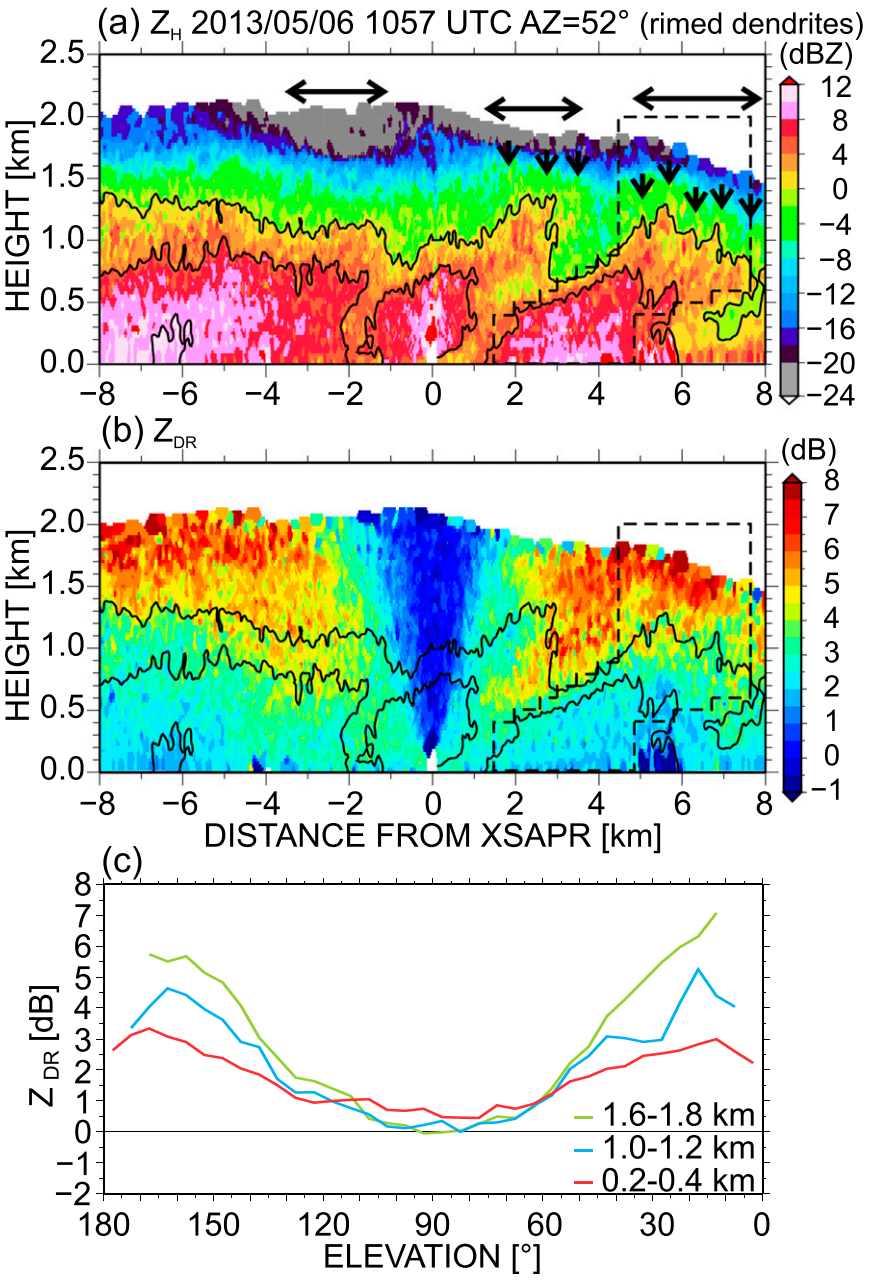


FIG. 13. As in Fig. 6, but for the rimed dendrite case at 1057 UTC 6 May 2013. The horizontal and vertical arrows in (a) denote large-scale and small-scale structures, respectively, as mentioned in the text. The black contour in (b) represents isolines of $Z_H$ every 4 dBZ from 0 dBZ. Lines in (c) represent heights of 0.2–0.4 km (red), 1.0–1.2 km (blue), and 1.6–1.8 km (green). The regions enclosed by dashed lines in (a) and (b) are used for mean profiles in Fig. 17, below.

maximum dimension $D$ of 4.0 mm, but with different thickness $T$ and projected area $A$, and hence mass $M$, were selected to illustrate the effects of aspect ratio and sparseness of ice in the crystal structure on the $\sigma_{hh}/\sigma_{vv}$ dependence. The aspect ratio AR is defined as a ratio of the length of the $c$ axis (thickness) to the length of the $a$ axis (maximum dimension). We also define a bulk density $\rho$ for each of four dendrites by assuming a spheroidal volume $V$:

$$V = \frac{\pi}{6} D^2 T. \tag{4}$$

The bulk density estimated from the spheroidal volume and mass is useful for relative comparisons between the

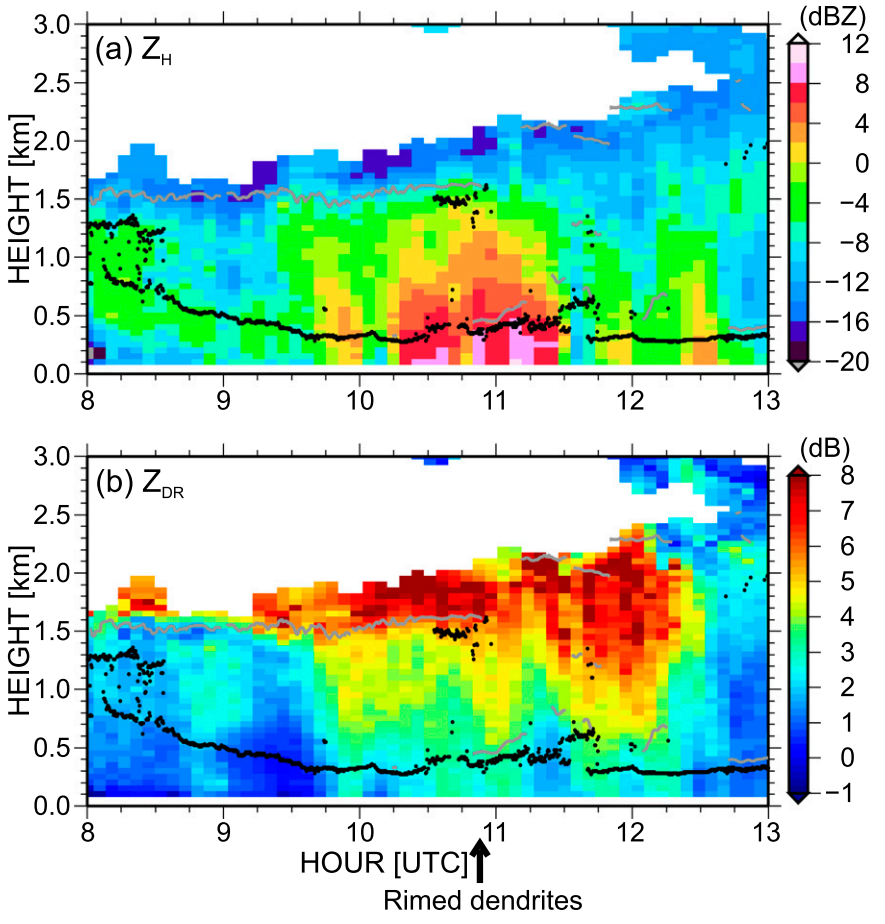


FIG. 14. As in Fig. 7, but for 6 May 2013.

four dendrites. The results from these four particles span approximately the full range of results from the full database.

The general elevation dependencies of $\sigma_{hh}/\sigma_{vv}$ match the expected values (for oblate spheroids) given by Ryzhkov et al. (2005):

$$Z_{dr}(\beta) = \frac{Z_{dr}(\beta = 0)}{\{[Z_{dr}(\beta = 0)]^{1/2} \sin^2\beta + \cos^2\beta\}^2}, \qquad (5)$$

where $\beta$ is antenna elevation angle and $Z_{dr}$ is linear differential reflectivity. For a given maximum dimension and aspect ratio, $\sigma_{hh}/\sigma_{vv}$ increases as the bulk density of a crystal increases when open spaces in the dendrite structure are filled and the dendrite appears more platelike (crystals 1, 2, and 3; see also Vivekanandan et al. 1994). The calculated maximum $\sigma_{hh}/\sigma_{vv}$ values (6.3–8.7 dB at elevation angles $< 20°$) and $\sigma_{hh}/\sigma_{vv}$ elevation dependence for the more filled-in dendrites (crystals 1 and 2) are in good agreement with the radar-measured $Z_{DR}$ in dendrite-dominated radar volumes [cf. Fig. 15b with Figs. 6c, 9c (1.2–1.4 km) and Fig. 13c (1.6–1.8 km)]. Similar maximum $\sigma_{hh}/\sigma_{vv}$ values (at low elevation angles; ~9 dB) and strong elevation dependencies were produced by the scatting calculations for small, compact platelike crystals.

We also use the four dendrites to examine the effect of light riming on $Z_{DR}$. Rime growth generally occurs on the crystal basal face and increases the aspect ratio. An increase in aspect ratio of an otherwise identical crystal results in a $\sigma_{hh}/\sigma_{vv}$ decrease (e.g., crystals 3 and 4) with little change in bulk density calculated from Eq. (4). However, rime growth may also fill open space in the dendrite structure, the effect of which is to increase the bulk density and hence $\sigma_{hh}/\sigma_{vv}$. There is little observational evidence which of these offsetting effects on $Z_{DR}$ dominate, and the net result may well be a function of the state of riming. For comparison, we show the measured $Z_{DR}$ elevation angle dependence observed at low levels when rimed crystals were dominated at the surface (Fig. 15b; dashed line).

The $\sigma_{hh}/\sigma_{vv}$ values at 0° elevation angle for all aggregates in the database are presented in Fig. 16 as a

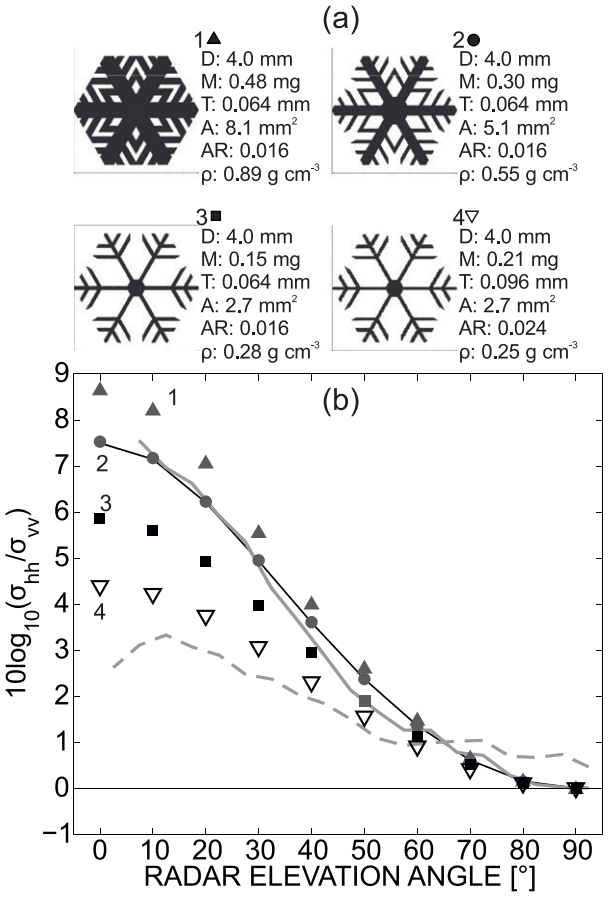


FIG. 15. Results from pristine dendrite scattering calculations for the four dendrites from the database. (a) The four representative dendrites, and their (b) ratios of horizontal to vertical backscattering cross sections $\sigma_{hh}/\sigma_{vv}$ as a function of elevation angle. The maximum dimension $D$, mass $M$, thickness $T$, project area $A$, and aspect ratio AR ($T/D$) for each dendrite are specified. The bulk density $\rho$ is estimated by assuming a spheroidal volume [Eq. (4)]. Dendrites 3 and 4 are the same in every respect other than thickness. The thickness of dendrite 4 is approximately 1.5 times that of dendrite 3. Gray lines in (b) are the observed $Z_{DR}$ profiles from the pristine dendrites (solid; height of 1.3–1.5 km and elevation angles of 90°–180°) and rimed dendrites (dashed; height of 0.2–0.4 km and elevation angles of 90°–180°) cases. The black line represents Eq. (5) with $Z_{dr}$ ($\beta$ = 0) = 5.623 (7.5 dB).

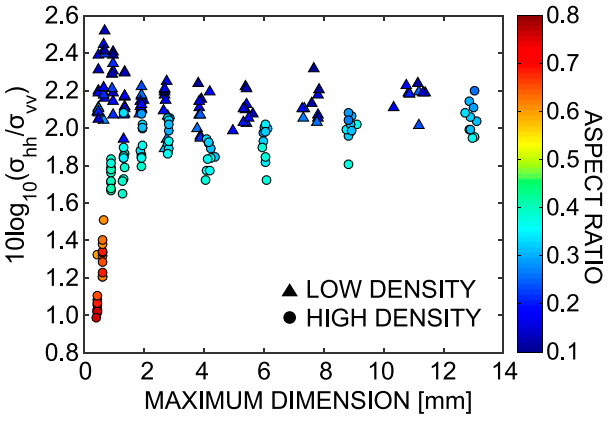


FIG. 16. Calculated $10\log_{10}(\sigma_{hh}/\sigma_{vv})$ at 0° elevation angle for all aggregates of dendrites in the database as a function of mass–dimensional relationship, maximum dimension, and aspect ratio. The color shading indicates aspect ratio. Triangles and circles represent low-density [according to Kajikawa (1989)] and high-density [according to Mitchell et al. (1990)] aggregates, respectively.

function of mass–dimensional relationship, maximum dimension, and aspect ratio. The aggregates conform to low- (Kajikawa 1989) and high-density (Mitchell et al. 1990) mass–dimensional relationships used to represent aggregates in a cloud-resolving model study of a shallow Arctic precipitating system (Avramov et al. 2011). The aggregates retain roughly oblate shapes with major axes aligned close to the horizontal plane [see Fig. 6 of Botta et al. (2011)] and are representative of light-to-moderate aggregation. The low-density aggregates have lower aspect ratios than the high-density aggregates and produce the highest $\sigma_{hh}/\sigma_{vv}$ values. For larger aggregates (>3 mm), the difference in $\sigma_{hh}/\sigma_{vv}$ between the two classes is small, with the $\sigma_{hh}/\sigma_{vv}$ values ranging from 1.7 to 2.4 dB. These values are in close agreement with the radar-measured $Z_{DR}$ values for the aggregate case in the lowest heights of 0.1–0.3 km at lower elevation angles (Fig. 9c) and stand in contrast to midlatitude observations of $Z_{DR}$ in aggregate-dominated regions (0.1–0.2 dB; e.g., Hall et al. 1984; Ryzhkov and Zrnić 1998; Ryzhkov et al. 2005; Kennedy and Rutledge 2011; Bechini et al. 2013). Potential causes for this difference are discussed in the following section.

## 5. Discussion

We presented three long-lasting cases with approximately steady state $Z_H$ and $Z_{DR}$ profiles in weakly forced shallow precipitating systems. In each case, ice particles from seeder clouds at the top of the system fell into at least one liquid-cloud layer embedded in the ice precipitating cloud systems. The seeder cloud and embedded liquid-cloud layer temperatures were between −14° and −18°C (Figs. 4, 11), with the liquid-cloud layers closer to −15°C. At these temperatures and liquid saturation, dendrites or sector plates are expected to be the dominant ice crystal habits (Magono and Lee 1966; Bailey and Hallett 2009). Despite these similarities between the precipitating systems, the $Z_H$ and $Z_{DR}$ structures and photographs of precipitation particles suggest different dominant precipitation production mechanisms for the cases: vapor deposition, aggregation, and riming.

To facilitate the discussion of differences in polarimetric signatures between the three cases, we constructed

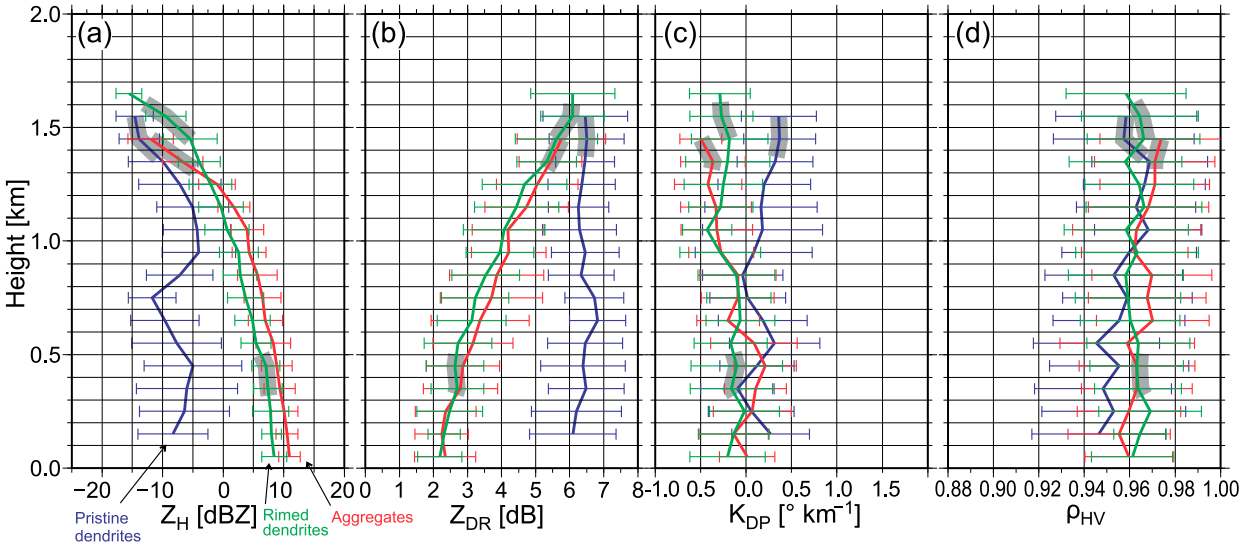


FIG. 17. Vertical profiles of averaged (a) $Z_H$, (b) $Z_{DR}$, (c) $K_{DP}$, and (d) $\rho_{HV}$ from the X-SAPR HRHIs, during which the pristine dendrites (blue line), aggregates (red line), and rimed dendrites (green line) were observed at the ground. The averaging areas are presented in Figs. 6, 9, and 13. Averages were calculated in 100-m altitude increments from all values with elevation angles <20° or >160°. The total number of samples in each profile exceeds 1900. Error bars represent standard deviations. Gray shading represents layers between ceilometer-measured cloud base and topmost liquid-cloud top.

mean profiles of $Z_H$, $Z_{DR}$, $K_{DP}$, and $\rho_{HV}$ through areas where the $Z_H$ and $Z_{DR}$ profiles are consistent with the time-evolving structures revealed in Figs. 7 and 14. These mean profiles (Fig. 17) come from blocks in a single HRHI for each case. Averages were calculated in 100-m altitude increments from values with elevation angles <20° or >160°. Because $Z_H$ in the HRHI of the aggregate case is mostly horizontally uniform, the block placement is not critical (Figs. 9a,b), but the HRHIs of the dendrite and riming cases exhibit some inhomogeneities that must be considered. For the pristine dendrite case, we selected two regions with lower $Z_H$ and higher $Z_{DR}$ (Figs. 6a,b), and for the rimed dendrite case, we followed one of the larger-scale structures from the cloud top to the surface (Figs. 13a,b). Because the X-SAPR is less sensitive than the KAZR, it frequently failed to detect the seeder clouds. Therefore, we also constructed mean profiles of the KAZR reflectivity and Doppler velocity for the three cases (Figs. 18a,b). Finally, we also present the HSRL linear depolarization and backscatter profiles (Figs. 18c,d). The selection of KAZR and HSRL averaging periods for each case followed the arguments presented for the HRHI blocks. Profiles for the pristine dendrite case were calculated for a period of weak reflectivity (Fig. 5c), for the rimed dendrite case following a precipitation streak (Fig. 12c) and for the aggregate case around the time of the photographs (Fig. 8a). Note that we named each profile according to the type of ice particles observed at the surface.

The X-SAPR and KAZR mean reflectivity profiles have the same general characteristics (Figs. 17a, 18a), but the KAZR indicate cloud-top reflectivities of −30 dB$Z$ about 200–300 m higher than the X-SAPR in all the cases, because the X-SAPR sensitivity (sensitivity ~−38 dB at 1 km) is lower than the KAZR (sensitivity ~−45 dB at 1 km). The mean Doppler velocities near the ground support our differentiation between the cases as pristine dendrites, rimed dendrites, and aggregates of dendrites. The mean Doppler velocities for each case correspond to particle fall speeds of "unrimed dendrites" and "densely rimed dendrites" [underlying crystal structure visible (from Locatelli and Hobbs 1974)] and "early snowflakes" (from Kajikawa 1989), respectively.

We use the mean KAZR reflectivities just above the tops of the liquid-cloud layers to quantify the seeder-cloud precipitation because of the KAZR's greater sensitivity. Figure 18a reveals systematic differences in the seeder-cloud layers between the three cases, with the pristine dendrite case having the lowest reflectivities (~−25 dB$Z$), the aggregate case higher (~−12 dB$Z$), and the riming case the highest (~−9 dB$Z$). Reflectivities in the liquid-cloud layers exceed the X-SAPR $Z_H$ minimum values, allowing us to use the X-SAPR values in and below these layers. The mean $Z_{DR}$ values in the upper liquid-cloud layers are similar for the three cases (>6 dB; Fig. 17b). Figures 5 and 12 show $Z_{DR}$ values above the upper-level liquid-cloud layers exceeding 8 dB for all three cases. These $Z_{DR}$ values and the seeder-cloud

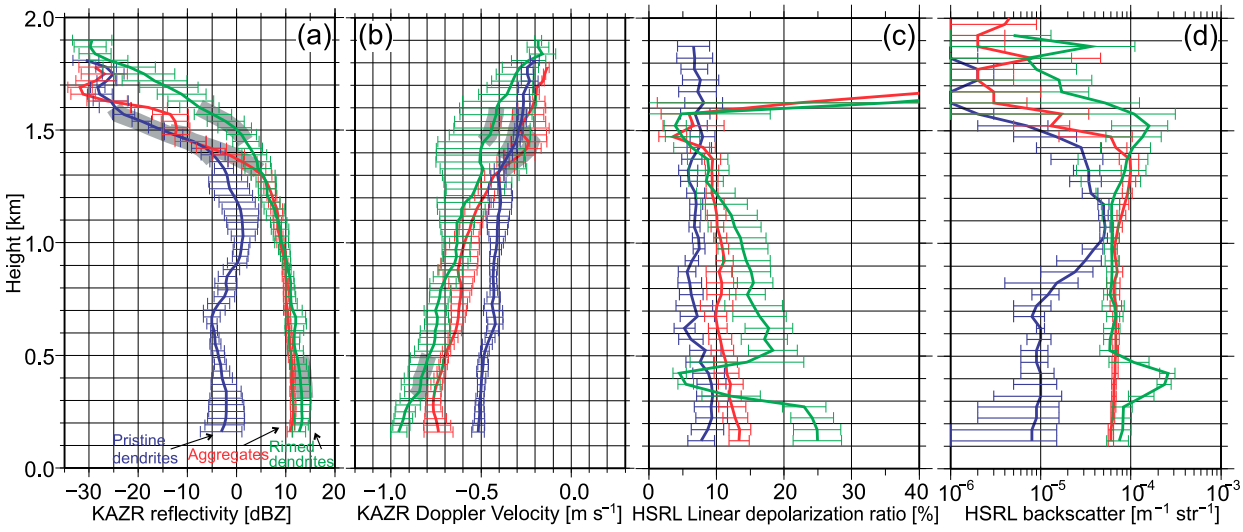


FIG. 18. As in Fig. 17, but for (a) radar reflectivity and (b) mean Doppler velocity from the KAZR, and (c) linear depolarization ratio and (d) backscatter from the HSRL. Negative Doppler velocities indicate downward motion. Areas for the averages are presented in Figs. 5, 8, and 12. Averages for (a),(b) and (c),(d) are calculated in 30- and 50-m altitude increments, respectively. The KAZR and HSRL profiles are averaged over 7 min, during which time period KAZR collected 120 profiles and HSRL collected 168.

temperatures suggest that highly oriented planar crystals dominated in the precipitation, falling into the liquid-cloud layers. In the liquid-cloud layers, vapor depositional growth of these crystals would tend to enhance dendritic habits because of the highly saturated conditions. The low LWP and the thin liquid-cloud layers during the pristine dendrite and aggregate cases on 2 May (Fig. 3b) suggest that rime growth, if present, was limited.

The X-SAPR $Z_H$ values rapidly increase by 6–12 dB within the liquid-cloud layers for both 2 May cases, with the larger increase occurring in the aggregate case (Fig. 17a). At the same height range, the $Z_{DR}$ decreases in the aggregate case but holds approximately steady in the pristine dendrite case, suggesting different ice particle growth processes for the reflectivity increases. The high $Z_{DR}$ and low HSRL linear depolarization ratio of the pristine dendrite case are indicative of large planar crystals, whereas the low $Z_H$ indicates low number concentrations of those crystals. Relative to the pristine dendrite case, Fig. 7 shows that the aggregate case seeder-cloud $Z_H$ intensified in association with an increase in cloud-top height, but $Z_{DR}$ remained high. The increasing $Z_H$ with constant $Z_{DR}$ suggests that higher number concentrations of ice particles precipitated from this deeper seeder cloud compared to the pristine dendrite case. Higher number concentrations of dendritic ice crystals can be more conducive to aggregation, owing to higher probabilities of ice crystals colliding with each other. The seeder-cloud precipitation characteristics may then explain the change in dominant precipitation production mechanism from vapor deposition to aggregation-dominated growth as indicated by the $Z_{DR}$ profile differences between the cases (Fig. 17b). Below the liquid-cloud layer, $Z_H$ continues to increase and $Z_{DR}$ decrease for the aggregate case, suggesting continued aggregation outside the liquid-cloud layer (e.g., Hall et al. 1984; Kennedy and Rutledge 2011; Andrić et al. 2013). This seeder-cloud impact carries through to the sub-liquid layer, as evidenced by the continued decrease of $Z_{DR}$ in the aggregate case. A closer look at Fig. 6 ($[x, z] = [-7\,\text{km}, 0.6\,\text{km}], [-1\,\text{km}, 1.1\,\text{km}]$) and Fig. 5b (1510 and 1630 UTC) reveals evidence of some periods of aggregation during the dendrite case as the $Z_{DR}$ decrease in small pockets for short periods even during the vapor-growth-dominated period.

The $Z_H$ and $Z_{DR}$ profiles of the rimed dendrite case (Figs. 17a,b) are similar to the aggregate case, with rapid in-cloud increase in $Z_H$ and decrease in $Z_{DR}$ and with continued increase in $Z_H$ and decrease in $Z_{DR}$ below the liquid-cloud layer until the top of the 0.5-km liquid water cloud. In the lower 500 m above the surface, $Z_{DR}$ remains approximately constant. The $Z_{DR}$ values for both cases attain 2–2.5 dB near the surface (Fig. 17b). The similarity of the X-SAPR $Z_H$ and $Z_{DR}$ profiles for the riming and aggregation cases suggests that auxiliary information is necessary to differentiate between the two processes.

Some differentiation between the aggregate and riming processes can be found in the mean Doppler velocity profiles observed by the zenith-pointing KAZR (Fig. 18b), but the biggest differences are found in the HSRL linear depolarization (Fig. 18c). The riming case

seeder-cloud precipitation has faster fall speeds ($+0.1\,\mathrm{m\,s^{-1}}$) and higher reflectivities (KAZR and X-SAPR; +5 dB$Z$) than the aggregation case but similar $Z_{DR}$ (X-SAPR). The fall speed depends on the mass and projected cross-sectional area, reflectivity on the mass and bulk density of individual ice particles and their number concentrations, and $Z_{DR}$ on the shape and bulk density of the ice particles. The observed differences suggest that more filled-in dendrites or plates fell into the upper liquid-cloud layer of the riming case than the aggregate case. Between the embedded liquid-cloud layers, the only available ice growth mechanisms are vapor deposition and aggregation. The riming case reflectivity increased by 10 dB with decreasing $Z_{DR}$ as ice particles fell through the region between the two embedded liquid-cloud layers (Figs. 17a, 18a). This increase suggests an active aggregation process even while the riming case maintained an $\sim 0.1\,\mathrm{m\,s^{-1}}$ fall speed advantage over the aggregate case (Fig. 18b). Differences in aggregate characteristics between the cases are revealed in the HSRL linear depolarization that increased toward the surface in the riming case but remained approximately constant in the aggregation case (Figs. 18c,d). The cause of these differences is difficult to determine from the available measurements, but we can offer a speculative suggestion that continued vapor depositional growth on lightly rimed hydrometeors increased surface irregularities on individual ice crystals, producing high depolarization. Near the surface, the mean KAZR reflectivities of the two cases were similar ($\sim$12 dB$Z$), but the mean fall speeds in the riming case increased, consistent with more dense, compact particles. The HSRL linear depolarization increased by $\sim$10% across the liquid-cloud layer, consistent with expected linear depolarization increasing upon riming (Sassen 1991). Zawadzki et al. (2001) observed downward velocities increasing by approximately 1–2 $\mathrm{m\,s^{-1}}$ over depths of 1–1.5 km for heavy riming cases in midlatitude precipitation systems. Although the increment in fall speed in the current study is smaller than the midlatitude cases, the specific increment is similar ($\sim 0.1\,\mathrm{m\,s^{-1}}$ per 100 m). These results suggest that, while some riming may have occurred in the upper (1.5 km) liquid-cloud layer, most of it took place as the ice passed through the lower (0.5 km) liquid-cloud layer. The magnitude of the KAZR Doppler velocity and the HSRL depolarization for the rimed dendrite case still increased slightly even below the lower liquid-cloud layer, suggesting that some aggregation occurred.

The mean profiles of $K_{DP}$ and $\rho_{HV}$ do not have the systematic enhancement in the high-$Z_{DR}$ regions often observed in midlatitude cases (Figs. 17c,d; Andrić et al. 2013; Bechini et al. 2013). In these shallow Arctic clouds with often-low ice particle number concentrations and ice water content, $K_{DP}$ may not have significant values because there is not enough accumulation of differential phase shift with propagation to be detectable with reasonable range smoothing. For the three low-$Z_H$ cases in this study, $K_{DP}$ fluctuated about $0^\circ\,\mathrm{km^{-1}}$ with considerable standard deviation. The low $\rho_{HV}$ values observed in the three cases are consistent with what may be expected from highly oriented, oblate particles (i.e., pristine dendrites, early stage aggregates, and rimed dendrites) in this study (Jameson 1989). The pristine dendrite case has the lowest mean $\rho_{HV}$; however, the large standard deviations about the mean prevent any firm conclusions.

The $Z_{DR}$ values for the pristine dendrite (>6 dB) and aggregate (2–2.5 dB) cases (Figs. 6, 7, 9, 15, 16, and 17b) are higher than those reported for dendrites in midlatitude clouds [0.5–4 dB for dendrites (Hall et al. 1984; Westbrook and Illingworth 2013; Schuur et al. 2012; Bechini et al. 2013; Schneebeli et al. 2013) and 0.1–0.2 dB for aggregates (Hall et al. 1984; Ryzhkov and Zrnić 1998; Ryzhkov et al. 2005; Kennedy and Rutledge 2011; Bechini et al. 2013)]. The focus of these midlatitude studies has been on higher $Z_H$ (15–30 dB$Z$) regions in deep precipitating systems. In such systems, the ice crystal concentrations are typically much higher than in the shallow Arctic clouds, and therefore they have more favorable conditions for aggregation. The coexistence of aggregates with dendrites will tend to reduce the $Z_{DR}$. The lower $Z_{DR}$ values in aggregate-dominated scatter are attributed to the very low bulk densities of aggregates and tumbling fall motions that produce a mean shape for the aggregates in the radar volume with aspect ratio close to 1 (e.g., Thompson et al. 2014).

In contrast, in the lower $Z_H$ (mostly <12 dB$Z$) clouds in this study, where the aggregation process is less efficient, owing to lower ice crystal concentrations, many of the aggregates consisted of only a few dendrites (Fig. 2d). During these early stages of aggregation, the aggregates retain more oblate shapes, consistent with the aggregate model used in the scattering calculations (Fig. 16). Botta et al. (2011) developed that model specifically for applications in shallow Arctic precipitating systems. The agreement between the calculated and measured $Z_{DR}$ values (close to the surface, Fig. 17b for aggregates) was attained without taking canting into consideration.

The aggregate $Z_{DR}$ calculations can be evaluated using the observed $Z_H$ (assuming 10 dB$Z$; Fig. 17a) and $Z_{DR}$ (2.3 dB; Fig. 17b) values just above the surface. Assuming only pristine dendrites and aggregates in the volume, the total reflectivity $Z_h^T = Z_h^A + Z_h^D$, where

superscripts $A$ and $D$ indicate the aggregate and pristine dendrite contributions, respectively, and $T$ the total reflectivity (all reflectivities in linear scales, as indicated by lowercase subscripts). Setting $f$ as the aggregate fraction of the total reflectivity, the total differential reflectivity $Z_{\rm dr}^T$ can be written as

$$Z_{\rm dr}^T = \left[\frac{f}{Z_{\rm dr}^A} + \frac{(1-f)}{Z_{\rm dr}^D}\right]^{-1}. \quad (6)$$

The observed $Z_h$ and $Z_{\rm dr}$ values are assumed to be the combined aggregate and pristine dendrite contributions, or $Z_h^T$ and $Z_{\rm dr}^T$. Taking $Z_{\rm dr}^A = 1.58$ (2 dB) and $Z_{\rm dr}^D = 5.01$ (7 dB) as representative values from the scattering database, the aggregates would have to account for ~90% of the 10 dB$Z$ $Z_h^T$ (aggregate contribution of ~9.5 dB$Z$; pristine dendrite contribution of ~0 dB$Z$). Alternatively, taking typical midlatitude $Z_{\rm dr}^A$ values for aggregates (1.02 identical to 0.1 dB; e.g., Ryzhkov et al. 2005; Thompson et al. 2014) and keeping $Z_{\rm dr}^D$ at 7 dB would require approximately equal reflectivity contributions by the two populations (~7 dB$Z$). None of the observations provide separate estimates of the dendrite versus aggregate contributions to the total reflectivity. A measure of the relative contributions may be gained by looking at the $Z_{\rm DR}$ variation with $Z_H$ from the 5+ hours of HRHI data presented in Fig. 7. The mean $Z_{\rm DR}$, as a function of $Z_H$, decreases linearly from ~6 dB at $Z_H = -8$ dB$Z$ to ~3.5 dB at $Z_H = 8$ dB$Z$, after which $Z_{\rm DR}$ stays approximately constant with increasing $Z_H$. This $Z_{\rm DR}$ decrease with increasing $Z_H$ mirrors a diminished impact of pristine dendrites on the $Z_{\rm DR}$ during active aggregation. We conclude from these numbers that a 7-dB$Z$ contribution from the dendrites in the 2 May situation is highly unlikely. This conclusion suggests that the $Z_{\rm DR}$ value of 0.1 dB is too low to explain the present observations and hence that the aggregates fell as oriented, lower aspect ratio particles that experienced little reduction in their $Z_{\rm DR}$ from canting. The stable Arctic environment (e.g., Sedlar and Shupe 2014; Vihma et al. 2014) may reduce turbulence and hence be a contributing factor to the relatively higher $Z_{\rm DR}$ values reported here. Matrosov et al. (2005) and Matrosov (2007) suggested similar behavior for snowflakes falling in stable environments.

## 6. Conclusions

This study is an initial look at microphysical processes in shallow Arctic clouds using the new DOE ARM X-band polarimetric radar (X-SAPR) in conjunction with other DOE ARM measurements at Barrow. X-SAPR HRHI scans through typical shallow Arctic precipitation systems dominated by vapor depositional, riming, and aggregation growth of dendrites are used to illustrate the $Z_{\rm DR}$ signature of each of the three processes. In all three cases, low-$Z_H$ precipitation fell into supercooled liquid-cloud layer(s) embedded in shallow ice precipitating systems (cloud tops of 1.5–2 km) in a seeder–feeder scenario. The precipitation $Z_H$ of all the cases (mostly <12 dB$Z$) were lower than the typical midlatitude snowstorm cases (15–30 dB$Z$).

The $Z_{\rm DR} > 6$ dB was observed in each case close to the cloud top. These high $Z_{\rm DR}$ values were retained through most of the depth of the system for a 3-h period with low $Z_H$ (<~0– dB$Z$) during which vapor depositional growth of dendrites was the dominant ice growth. Scattering calculations showed that these $Z_{\rm DR}$ values are consistent with high-bulk-density dendrites. Aggregation increased $Z_H$ and decreased $Z_{\rm DR}$, with minimum $Z_{\rm DR}$ values of ~2 dB attained close to the surface. The relatively (to midlatitude observations) high $Z_{\rm DR}$ (2–3 dB) and low $Z_H$ attained by the aggregates are consistent with early stage aggregates falling with preferred horizontal orientation. The primary difference between the pristine dendrite and aggregate cases was found in the seeder-cloud $Z_H$. Higher $Z_H$ with similar $Z_{\rm DR}$ values indicate that higher number concentrations of ice particles seeded the liquid cloud below to produce conditions more conducive for aggregation. The low $Z_H$ and high $Z_{\rm DR}$ are indicative of low number concentrations of large dendrites. The observed cases illustrate that the intensity of seeding into the liquid-cloud layers can play an important role in the precipitation production mechanisms.

The X-SAPR $Z_{\rm DR}$ measurements were insufficient to distinguish riming from aggregation in this study. Consistent differences between the two cases were found in the vertically pointing Ka-band radar mean Doppler velocity (fall speed) and lidar linear depolarization. The mean fall speed in the riming case was 0.1 m s$^{-1}$ faster than the aggregation case and accelerated downward at ~0.1 m s$^{-1}$ per 100 m within a low-level liquid-cloud layer (150-m thickness). The lidar linear depolarization increased by ~10% across the liquid-cloud layer. Even with the full complement of DOE ARM measurements, it remains difficult to distinguish riming from aggregation in the weakly precipitating clouds.

This study documented the ability of the new X-SAPR polarimetric radar to study the microphysical processes operating in Arctic precipitation clouds. The clean Arctic environment can enhance $Z_{\rm DR}$ signals relative to more complex midlatitude cases, producing higher values. The value of the X-SAPR measurements

is increased when combined with other ARM instruments capable of detecting the low-reflectivity ice-generating mixed-phase clouds.

*Acknowledgments.* This research was supported by the U.S. Department of Energy's Atmospheric Science Program Atmospheric System Research, an Office of Science, Office of Biological and Environmental Research program, under Grants DE-FG02-05ER64058, DE-SC0008811, and ER65459. The authors thank Scott Giangrande, Edwin Eloranta, Eugene Clothiaux, and Kültegin Aydin for fruitful suggestions and comments. The authors also thank Mark Ivey and Nitin Bharadwaj for collecting radar data during the IOP and Maria Cadeddu for input on the LWP retrievals. Thanks are extended to the reviewers of this paper, whose comments helped to improve the manuscript. The High Spectral Resolution Lidar data were obtained from the University of Wisconsin Lidar Group (http://lidar.ssec.wisc.edu/index.htm).

## REFERENCES

Andrić, J., M. R. Kumjian, D. Zrnić, J. M. Straka, and V. Melnikov, 2013: Polarimetric signatures above the melting layer in winter storms: An observational and modeling study. *J. Appl. Meteor. Climatol.*, **52**, 682–700, doi:10.1175/JAMC-D-12-028.1.

Avramov, A., and Coauthors, 2011: Toward ice formation closure in Arctic mixed-phase boundary layer clouds during ISDAC. *J. Geophys. Res.*, **116**, D00T08, doi:10.1029/2011JD015910.

Aydin, K., and C. Tang, 1997: Millimeter wave radar scattering from model ice crystal distributions. *IEEE Trans. Geosci. Remote Sens.*, **35**, 140–146, doi:10.1109/36.551942.

Bailey, M. P., and J. Hallett, 2009: A comprehensive habit diagram for atmospheric ice crystals: Confirmation from the laboratory, AIRS II, and other fields. *J. Atmos. Sci.*, **66**, 2888–2899, doi:10.1175/2009JAS2883.1.

Bechini, R., L. Baldini, and V. Chandrasekar, 2013: Polarimetric radar observations in the ice region of precipitating clouds at C-band and X-band radar frequencies. *J. Appl. Meteor. Climatol.*, **52**, 1147–1169, doi:10.1175/JAMC-D-12-055.1.

Bharadwaj, N., K. B. Widener, K. L. Johnson, S. Collis, and A. Koontz, 2011: ARM radar infrastructure for global and regional climate study. *Proc. 35th Conf. on Radar Meteorology*, Pittsburgh, PA, Amer. Meteor. Soc., 16B.4. [Available online at https://ams.confex.com/ams/35Radar/webprogram/Paper191707.html.]

Bigg, E. K., 1996: Ice forming nuclei in the high Arctic. *Tellus*, **48B**, 223–233, doi:10.1034/j.1600-0889.1996.t01-1-00007.x.

Botta, G., K. Aydin, J. Verlinde, A. E. Avramov, A. S. Ackerman, A. M. Fridlind, G. M. McFarquhar, and M. Wolde, 2011: Milimeter wave scattering from ice crystals and their aggregates: Comparing cloud model simulations with X- and Ka-band radar measurements. *J. Geophys. Res.*, **116**, D00T04, doi:10.1029/2011JD015909.

——, ——, and ——, 2013: Variability in millimeter wave scattering properties of dendritic ice crystals. *J. Quant. Spectrosc. Radiat. Transfer*, **131**, 105–114, doi:10.1016/j.jqsrt.2013.05.009.

Bringi, V. N., and V. Chandrasekar, 2001: *Polarimetric Doppler Weather Radar: Principles and Applications.* Cambridge University Press, 636 pp.

——, T. A. Seliga, and S. M. Cherry, 1983: Statistical properties of the dual-polarization differential reflectivity ($Z_{DR}$) radar signal. *IEEE Trans. Geosci. Remote Sens.*, **GE-21**, 215–220, doi:10.1109/TGRS.1983.350491.

Cadeddu, M. P., D. D. Turner, and J. C. Liljegren, 2009: A neural network for real-time retrievals of PWV and LWP from Arctic millimeter-wave ground-based observations. *IEEE Trans. Geosci. Remote Sens.*, **47**, 1887–1900, doi:10.1109/TGRS.2009.2013205.

Curry, J. A., W. B. Rossow, D. Randall, and J. L. Schramm, 1996: Overview of Arctic clouds and radiation characteristics. *J. Climatol.*, **9**, 1731–1764, doi:10.1175/1520-0442(1996)009<1731:OOACAR>2.0.CO;2.

de Boer, G., E. W. Eloranta, and M. D. Shupe, 2009: Arctic mixed-phase stratiform cloud properties from multiple years of surface-based measurements at two high-latitude locations. *J. Atmos. Sci.*, **66**, 2874–2887, doi:10.1175/2009JAS3029.1.

Dolan, B., and D. A. Rutledge, 2009: A theory-based hydrometeor identification algorithm for X-band polarimetric radars. *J. Atmos. Oceanic Technol.*, **26**, 2071–2088, doi:10.1175/2009JTECHA1208.1.

Doviak, R. J., and D. S. Zrnić, 1993: *Doppler Radar and Weather Observations.* Dover Publications, 562 pp.

Eloranta, E. W., 2005: High spectral resolution lidar. *Lidar: Range-Resolved Optical Remote Sensing of the Atmosphere*, C. Weitkamp, Ed., Springer-Verlag, 143–163.

Fountain, A. G., and T. Ohtake, 1985: Concentrations and source areas of ice nuclei in the Alaskan atmosphere. *J. Climate Appl. Meteor.*, **24**, 377–382, doi:10.1175/1520-0450(1985)024<0377:CASAOI>2.0.CO;2.

Gourley, J. J., P. Tabary, and J. P. du Chatelet, 2006: Data quality of the Meteo-France C-band polarimetric radar. *J. Atmos. Oceanic Technol.*, **23**, 1340–1356, doi:10.1175/JTECH1912.1.

Hall, M. P. M., J. W. F. Goddard, and S. M. Cherry, 1984: Identification of hydrometeors and other targets by dual-polarization radar. *Radio Sci.*, **19**, 132–140, doi:10.1029/RS019i001p00132.

Hobbs, P. V., and A. L. Rangno, 1998: Microstructures of low and middle-level clouds over the Beaufort Sea. *Quart. J. Roy. Meteor. Soc.*, **124**, 2035–2071, doi:10.1002/qj.49712455012.

Hubbert, J. C., and V. N. Bringi, 1995: An iterative filtering technique for the analysis of copolar differential phase and dual-frequency radar measurements. *J. Atmos. Oceanic Technol.*, **12**, 643–648, doi:10.1175/1520-0426(1995)012<0643:AIFTFT>2.0.CO;2.

Intrieri, J. M., M. D. Shupe, T. Uttal, and B. J. McCarty, 2002: An annual cycle of Arctic cloud characteristics observed by radar and lidar at SHEBA. *J. Geophys. Res.*, **107**, 8030, doi:10.1029/2000JC000423.

Jameson, A. R., 1989: The interpretation and meteorological application of radar backscatter amplitude ratios at linear polarizations. *J. Atmos. Oceanic Technol.*, **6**, 908–919, doi:10.1175/1520-0426(1989)006<0908:TIAMAO>2.0.CO;2.

Jayaweera, K., and T. Ohtake, 1973: Concentration of ice crystals in Arctic stratus clouds. *J. Rech. Atmos.*, **7**, 199–207.

Kajikawa, M., 1989: Observation of the falling motion of early snowflakes. Part II: On the variation of falling velocity. *J. Meteor. Soc. Japan*, **67**, 731–738.

Kennedy, P. C., and S. A. Rutledge, 2011: S-band dual-polarization radar observations of winter storms. *J. Appl. Meteor. Climatol.*, **50**, 844–858, doi:10.1175/2010JAMC2558.1.

Kumjian, M. R., A. V. Ryzhkov, H. D. Reeves, and T. J. Schuur, 2013: Dual-polarization radar observations of hydrometeor refreezing in winter storms. *J. Appl. Meteor. Climatol.*, **52**, 2549–2566, doi:10.1175/JAMC-D-12-0311.1.

——, S. A. Rutledge, R. M. Rasmussen, P. C. Kennedy, and M. Dixon, 2014: High-resolution polarimetric radar observations of snow generating cells. *J. Appl. Meteor. Climatol.*, **53**, 1636–1658, doi:10.1175/JAMC-D-13-0312.1.

Liljegren, J. C., E. E. Clothiaux, G. G. Mace, S. Kato, and X. Dong, 2001: A new retrieval for cloud liquid water path using a ground-based microwave radiometer and measurements of cloud temperature. *J. Geophys. Res.*, **106**, 14 485–14 500, doi:10.1029/2000JD900817.

Liu, H., and V. Chandrasekar, 2000: Classification of hydrometeors based on polarimetric radar measurements: Development of fuzzy logic and neuro-fuzzy systems, and in situ verification. *J. Atmos. Oceanic Technol.*, **17**, 140–164, doi:10.1175/1520-0426(2000)017<0140:COHBOP>2.0.CO;2.

Locatelli, J. D., and P. V. Hobbs, 1974: Fall speeds and masses of solid precipitation particles. *J. Geophys. Res.*, **79**, 2185–2197, doi:10.1029/JC079i015p02185.

Lu, Y., E. E. Clothiaux, K. Aydin, and J. Verlinde, 2014: Dielectric constant adjustments in computations of the scattering properties of solid ice crystals using the Generalized Multi-particle Mie method. *J. Quant. Spectrosc. Radiat. Transfer*, **135**, 1–8, doi:10.1016/j.jqsrt.2013.12.005.

Magono, C., and C. W. Lee, 1966: Meteorological classification of natural snow crystals. *J. Fac. Sci. Hokkaido Univ., Ser. VII*, **2**, 321–335.

Matrosov, S. Y., 1991: Theoretical study of radar polarization parameters obtained from cirrus clouds. *J. Atmos. Sci.*, **48**, 1062–1070, doi:10.1175/1520-0469(1991)048<1062:TSORPP>2.0.CO;2.

——, 2007: Modeling backscatter properties of snowfall at millimeter wavelengths. *J. Atmos. Sci.*, **64**, 1727–1736, doi:10.1175/JAS3904.1.

——, R. F. Reinking, R. A. Kropfli, B. E. Martner, and B. W. Bartram, 2001: On the use of radar depolarization ratios for estimating shapes of ice hydrometeors in winter clouds. *J. Appl. Meteor.*, **40**, 479–490, doi:10.1175/1520-0450(2001)040<0479:OTUORD>2.0.CO;2.

——, ——, and I. V. Djalalova, 2005: Inferring fall attitudes of pristine dendritic crystals from polarimetric radar data. *J. Atmos. Sci.*, **62**, 241–250, doi:10.1175/JAS-3356.1.

McFarquhar, G. M., G. Zhang, M. R. Poellot, G. L. Kok, R. McCoy, T. Tooman, A. Fridlind, and A. J. Heymsfield, 2007: Ice properties of single-layer stratocumulus during the Mixed-Phase Arctic Cloud Experiment: 1. Observations. *J. Geophys. Res.*, **112**, D24201, doi:10.1029/2007JD008633.

Mitchell, D. L., R. Zhang, and R. L. Pitter, 1990: Mass-dimensional relationships for ice particles and the influence of riming on snowfall rates. *J. Appl. Meteor.*, **29**, 153–163, doi:10.1175/1520-0450(1990)029<0153:MDRFIP>2.0.CO;2.

Morrison, H., P. Zuidema, G. M. McFarquhar, A. Bansemer, and A. J. Heymsfield, 2011: Snow microphysical observations in shallow mixed-phase and deep frontal Arctic cloud systems. *Quart. J. Roy. Meteor. Soc.*, **137**, 1589–1601, doi:10.1002/qj.840.

——, G. Boer, G. Feingold, J. Harrington, M. D. Shupe, and K. Sulia, 2012: Resilience of persistent Arctic mixed-phase clouds. *Nat. Geosci.*, **5**, 11–17, doi:10.1038/ngeo1332.

Oue, M., M. R. Kumjian, Y. Lu, Z. Jiang, E. E. Clothiaux, J. Verlinde, and K. Aydin, 2015: X-band polarimetric and Ka-band Doppler spectral radar observations of a graupel-producing Arctic mixed-phase cloud. *J. Appl. Meteor. Climatol*, **54**, 1335–1351, doi:10.1175/JAMC-D-14-0315.1.

Park, H. S., A. V. Ryzhkov, D. S. Zrnić, and K.-E. Kim, 2009: The hydrometeor classification algorithm for the polarimetric WSR-88D: Description and application to an MCS. *Wea. Forecasting*, **24**, 730–748, doi:10.1175/2008WAF2222205.1.

Pinto, J. O., J. A. Curry, and J. M. Intrieri, 2001: Cloud–aerosol interactions during autumn over Beaufort Sea. *J. Geophys. Res.*, **106**, 15 077–15 097, doi:10.1029/2000JD900267.

Platt, C. M. R., 1978: Lidar backscatter from horizontal ice crystal plates. *J. Appl. Meteor.*, **17**, 482–488, doi:10.1175/1520-0450(1978)017<0482:LBFHIC>2.0.CO;2.

Prenni, A. J., P. Demott, D. C. Rogers, A. M. Kreidenweis, G. M. McFarquhar, G. Zhang, and M. R. Poellot, 2009: Ice nuclei characteristics from M-PACE and their relation to ice formation in clouds. *Tellus*, **61B**, 436–448, doi:10.1111/j.1600-0889.2009.00415.x.

Radke, L. F., P. V. Hobbs, and J. E. Pinnons, 1976: Observations of cloud condensation nuclei, sodium-containing particles, ice nuclei and the light-scattering coefficient near Barrow, Alaska. *J. Appl. Meteor.*, **15**, 982–995, doi:10.1175/1520-0450(1976)015<0982:OOCCNS>2.0.CO;2.

Ryzhkov, A. V., and D. S. Zrnić, 1998: Discrimination between rain and snow with a polarimetric radar. *J. Appl. Meteor.*, **37**, 1228–1240, doi:10.1175/1520-0450(1998)037<1228:DBRASW>2.0.CO;2.

——, S. E. Giangrande, V. M. Melnikov, and T. J. Schuur, 2005: Calibration issues of dual-polarization radar measurements. *J. Atmos. Oceanic Technol.*, **22**, 1138–1155, doi:10.1175/JTECH1772.1.

——, P. Zhang, H. D. Reeves, M. R. Kumjian, T. Tschallener, S. Troemel, and C. Simmer, 2016: Quasi-vertical profiles—A new way to look at polarimetric radar data. *J. Atmos. Oceanic Technol.*, doi:10.1175/JTECH-D-15-0020.1, in press.

Sassen, K., 1991: The polarization lidar technique for cloud research: A review and current assessment. *Bull. Amer. Meteor. Soc.*, **72**, 1848–1866, doi:10.1175/1520-0477(1991)072<1848:TPLTFC>2.0.CO;2.

——, and S. Benson, 2001: A midlatitude cirrus cloud climatology from the facility for atmospheric remote sensing. Part II: Microphysical properties derived from lidar depolarization. *J. Atmos. Sci.*, **58**, 2103–2112, doi:10.1175/1520-0469(2001)058<2103:AMCCCF>2.0.CO;2.

Schneebeli, M., N. Dawes, M. Lehning, and A. Berne, 2013: High-resolution vertical profiles of X-band polarimetric radar observables during snowfall in the Swiss Alps. *J. Appl. Meteor. Climatol.*, **52**, 378–394, doi:10.1175/JAMC-D-12-015.1.

Schrom, R. S., M. R. Kumjian, and Y. Lu, 2015: Polarimetric radar signatures of dendritic growth zones within Colorado winter storms. *J. Appl. Meteor. Climatol.*, **54**, 2365–2388, doi:10.1175/JAMC-D-15-0004.1.

Schuur, T., A. Ryzhkov, D. Forsyth, and H. Reeves, 2012: Precipitation observations with NSSL's X-band polarimetric radar during the SNOW-V10 campaign. *Pure Appl. Geophys.*, **171**, 95–112, doi:10.1007/s00024-012-0569-2.

Sedlar, J., and M. D. Shupe, 2014: Characteristic nature of vertical motions observed in Arctic mixed-phase stratocumulus. *Atmos. Chem. Phys.*, **14**, 3461–3478, doi:10.5194/acp-14-3461-2014.

Seliga, T. A., and V. N. Bringi, 1976: Potential use of radar differential reflectivity measurements at orthogonal polarizations for measuring precipitation. *J. Appl. Meteor.*, **15**, 69–76, doi:10.1175/1520-0450(1976)015<0069:PUORDR>2.0.CO;2.

——, ——, and H. H. Al-Khatib, 1981: A preliminary study of comparative measurements of rainfall rate using the differential reflectivity radar technique and a raingage network. *J. Appl. Meteor.*, **20**, 1362–1368, doi:10.1175/1520-0450(1981)020<1362:APSOCM>2.0.CO;2.

Shupe, M. D., P. Kollias, S. Y. Matrosov, and T. L. Schneider, 2004: Deriving mixed-phase cloud properties from Doppler radar spectra. *J. Atmos. Oceanic Technol.*, **21**, 660–670, doi:10.1175/1520-0426(2004)021<0660:DMCPFD>2.0.CO;2.

——, S. Y. Matrosov, and T. Uttal, 2006: Arctic mixed-phase cloud properties derived from surface-based sensors at SHEBA. *J. Atmos. Sci.*, **63**, 697–711, doi:10.1175/JAS3659.1.

——, and Coauthors, 2008a: A focus on mixed-phase clouds. *Bull. Amer. Meteor. Soc.*, **89**, 1549–1562, doi:10.1175/2008BAMS2378.1.

——, P. Kollias, P. O. G. Persson, and G. M. McFarquhar, 2008b: Vertical motions in Arctic mixed-phase stratiform clouds. *J. Atmos. Sci.*, **65**, 1304–1322, doi:10.1175/2007JAS2479.1.

Straka, J. M., and D. S. Zrnić, 1993: An algorithm to deduce hydrometeor types and contents from multiparameter radar data. Preprints, *26th Conf. on Radar Meteorology*, Norman, OK, Amer. Meteor. Soc., 513–516.

Thompson, E. J., S. A. Rutledge, B. Dolan, V. Chandrasekar, and B. L. Cheong, 2014: A dual-polarization radar hydrometeor classification algorithm for winter precipitation. *J. Atmos. Oceanic Technol.*, **31**, 1457–1481, doi:10.1175/JTECH-D-13-00119.1.

Turner, D. D., 2005: Arctic mixed-phase cloud properties from AERI lidar observations: Algorithm and results from SHEBA. *J. Appl. Meteor.*, **44**, 427–444, doi:10.1175/JAM2208.1.

Verlinde, J., M. P. Rambukkange, E. E. Clothiaux, G. M. McFarquhar, and E. W. Eloranta, 2013: Arctic multilayered mixed-phase cloud processes revealed in millimeter-wave cloud radar Doppler spectra. *J. Geophys. Res.*, **118**, 13 199–13 213, doi:10.1002/2013JD020183.

Vihma, T., and Coauthors, 2014: Advances in understanding and parameterization of small-scale physical processes in the marine Arctic climate system: A review. *Atmos. Chem. Phys.*, **14**, 9403–9450, doi:10.5194/acp-14-9403-2014.

Vivekanandan, J., V. N. Bringi, M. Hagan, and P. Meischner, 1994: Polarimetric radar studies of atmospheric ice particles. *IEEE Trans. Geosci. Remote Sens.*, **32**, 1–10, doi:10.1109/36.285183.

——, S. M. Ellis, R. Oye, D. S. Zrnić, A. V. Ryzhkov, and J. Straka, 1999: Cloud microphysics retrieval using S-band dual-polarization radar measurements. *Bull. Amer. Meteor. Soc.*, **80**, 381–388, doi:10.1175/1520-0477(1999)080<0381:CMRUSB>2.0.CO;2.

Westbrook, C. D., 2014: Rayleigh scattering by hexagonal ice crystals and the interpretation of dual-polarization radar measurements. *Quart. J. Roy. Meteor. Soc.*, **140**, 2090–2096, doi:10.1002/qj.2262.

——, and A. J. Illingworth, 2013: The formation of ice in a long-lived supercooled layer cloud. *Quart. J. Roy. Meteor. Soc.*, **139**, 2209–2221, doi:10.1002/qj.2096.

Williams, E. R., and Coauthors, 2015: Measurements of differential reflectivity in snowstorms and warm season stratiform systems. *J. Appl. Meteor. Climatol.*, **54**, 573–595, doi:10.1175/JAMC-D-14-0020.1.

Witte, H. J., 1968: Airborne observations of cloud particles and infrared flux density (8–14 $\mu$) in the Arctic. M.S. thesis, Dept. of Atmospheric Sciences, University of Washington, 101 pp.

Wolde, M., and G. Vali, 2001: Polarimetric signatures from ice crystals observed at 95 GHz in winter clouds. Part I: Dependence on crystal form. *J. Atmos. Sci.*, **58**, 828–841, doi:10.1175/1520-0469(2001)058<0828:PSFICO>2.0.CO;2.

Xu, Y.-L., 1995: Electromagnetic scattering by an aggregate of spheres. *Appl. Opt.*, **34**, 4573–4588, doi:10.1364/AO.34.004573.

Zawadzki, I., F. Fabry, and W. Szyrmer, 2001: Observations of supercooled water and secondary ice generation by a vertically pointing X-band Doppler radar. *Atmos. Res.*, **59–60**, 343–359, doi:10.1016/S0169-8095(01)00124-7.

Zrnić, D. S., R. Raghavan, and V. Chandrasekar, 1994: Observation of copular correlation coefficient through a bright band at vertical incidence. *J. Appl. Meteor.*, **33**, 45–52, doi:10.1175/1520-0450(1994)033<0045:OOCCCT>2.0.CO;2.

——, A. Ryzhkov, J. Straka, Y. Liu, and J. Vivekanandan, 2001: Testing a procedure for automatic classification of hydrometeor types. *J. Atmos. Oceanic Technol.*, **18**, 892–913, doi:10.1175/1520-0426(2001)018<0892:TAPFAC>2.0.CO;2.